

# The Effect of Geometry, Spin, and Orbital Optimization in Achieving Accurate, Correlated Results for Iron–Sulfur Cubanes

Carlos Mejuto-Zaera,\* Demeter Tzeli, David Williams-Young, Norm M. Tubman,\* Mikuláš Matoušek, Jiri Brabec, Libor Veis,\* Sotiris S. Xantheas,\* and Wibe A. de Jong\*



Cite This: *J. Chem. Theory Comput.* 2022, 18, 687–702



Read Online

ACCESS |



Metrics & More

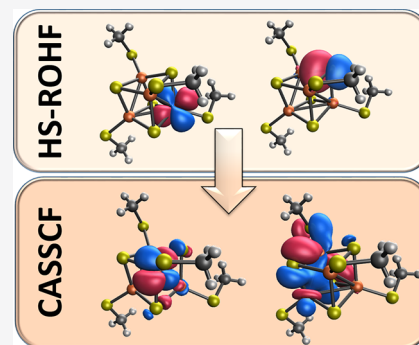


Article Recommendations



Supporting Information

**ABSTRACT:** Iron–sulfur clusters comprise an important functional motif in the catalytic centers of biological systems, capable of enabling important chemical transformations at ambient conditions. This remarkable capability derives from a notoriously complex electronic structure that is characterized by a high density of states that is sensitive to geometric changes. The spectral sensitivity to subtle geometric changes has received little attention from correlated, large active space calculations, owing partly to the exceptional computational complexity for treating these large and correlated systems accurately. To provide insight into this aspect, we report the first Complete Active Space Self Consistent Field (CASSCF) calculations for different geometries of the  $[\text{Fe}(\text{II/III})_4\text{S}_4(\text{SMe})_4]^{-2}$  clusters using two complementary, correlated solvers: spin-pure Adaptive Sampling Configuration Interaction (ASCI) and Density Matrix Renormalization Group (DMRG). We find that the previously established picture of a double-exchange driven magnetic structure, with minute energy gaps ( $<1$  mHa) between consecutive spin states, has a weak dependence on the underlying geometry. However, the spin gap between the singlet and the spin state  $2S + 1 = 19$ , corresponding to a maximal number of Fe-*d* electrons being unpaired and of parallel spin, is strongly geometry dependent, changing by a factor of 3 upon slight deformations that are still within biologically relevant parameters. The CASSCF orbital optimization procedure, using active spaces as large as 86 electrons in 52 orbitals, was found to reduce this gap compared to typical mean-field orbital approaches. Our results show the need for performing large active space calculations to unveil the challenging electronic structure of these complex catalytic centers and should serve as accurate starting points for fully correlated treatments upon inclusion of dynamical correlation outside the active space.



## 1. INTRODUCTION

Iron–sulfur clusters are ubiquitous. They are involved in many biological systems operating as active centers of proteins in essential life-sustaining processes such as photosynthesis, respiration, and nitrogen fixation.<sup>1–3</sup> They are involved in electron transfer processes,<sup>4,5</sup> substrate activation and binding,<sup>6,7</sup> catalytic reactions,<sup>8,9</sup> DNA repair,<sup>10</sup> signal transductions,<sup>11</sup> iron/sulfur storage,<sup>12</sup> regulation of gene expression,<sup>13</sup> and enzyme activity.<sup>14</sup> Additionally, they are significant in industrial catalysis.<sup>15,16</sup> The key factors for their remarkable reactivity, among others, are the small reorganization energy, the proper redox potentials, the flexibility of the cluster geometry, and the facile exchange of ligands.<sup>17,18</sup> Moreover, one of the properties underlying their remarkable reactivity is their low-lying, dense electronic state manifold. Therefore, it is of particular importance to understand the intrinsic electronic structure of the Fe–S clusters as well as its modification due to their surroundings, as prerequisites in order to interpret the functionality and properties of these complexes. As the result of the continuing interest in these iron–sulfur systems, several previous investigations have been reported.

There have been many computational studies reported for iron–sulfur clusters employing the Broken Symmetry analysis<sup>19</sup> of spin coupling, and especially the commonly used BS-DFT methodology, see for instance.<sup>20–24</sup> In general, this approach works quite well for the prediction of the geometry for molecular clusters involving multiple transition metals. However, it describes a weighted average over the (multiplet) states and as such it is not appropriate enough for the efficient calculation of the correlation energy of these multireference systems. Additionally, it depends on the density functional used.<sup>25</sup> Note that previous calculations on the  $[\text{Fe}_2\text{S}_2(\text{SCH}_3)_2]^{-2}$  and  $[\text{Fe}_4\text{S}_4(\text{SCH}_3)_4]^{-2}$  clusters indicated that both clusters have an unusually dense spectrum, which is different from the predictions of the Heisenberg double-exchange model.<sup>26</sup> Finally, it has been mentioned that BS-DFT

Received: August 17, 2021

Published: January 16, 2022



for reported FeIII complexes predicts some of the exchange couplings to be ferromagnetic, whereas the experimentally derived couplings are all antiferromagnetic; additionally, the best-fit exchange parameters can depend significantly on the set of spin configurations chosen.<sup>27</sup>

While both trinuclear  $[\text{Fe}_3\text{S}_4]$  and tetra-nuclear  $[\text{Fe}_4\text{S}_4]$  clusters are found in proteins, such as ferredoxins, and are both regarded as electron transfer sites in a variety of bacteria,<sup>28,29</sup> much attention has been mainly given to the  $[\text{Fe}_4\text{S}_4]$  clusters by applying mainly the BS-DFT methodology. To the best of our knowledge, there are only three previous theoretical studies where multireference methodologies, such as Density Matrix Renormalization Group (DMRG),<sup>26</sup> Coupled Cluster Valence Bond (CCVB),<sup>30</sup> and very recently FCIQMC,<sup>31</sup> have been applied to the  $[\text{Fe}_4\text{S}_4(\text{SCH}_3)_4]^{-2}$  cluster. It should also be noted that multireference methods, such as MC-PDFT, CASPT2/RASPT2, and NEVPT2, have been used for bimetallic Fe–S clusters.<sup>32</sup>

In this study, we report the results for the  $[\text{Fe}_4\text{S}_4(\text{SCH}_3)_4]^{-2}$  cluster using the Adaptive Sampling Configuration Interaction (ASCI) and DMRG methodologies. These are variational and complementary methods to treat strong correlation in many-body systems. They capture the static correlation, while extensions, such as ASCI plus second-order perturbation (ASCI+PT2) extrapolated results and DMRG with predefined very tight truncation error (TRE), are used to account for the dynamical correlation within the active space, estimating the Full Configuration Interaction (FCI) limit. We employ these approaches in large active space calculations. Besides gaining insight into the geometry dependence of the electronic structure of FeS cubanes beyond the accuracy of mean-field-like methods, our active space descriptions can serve as optimal starting points for fully correlated studies, including the dynamical correlation beyond the active space with methods, such as CASPT2 or NEVPT2. The significant challenge that these approaches represent brings their implementation beyond the scope of the current paper.

## 2. METHODS

To study the low energy eigenstates of iron–sulfur clusters, we employ the ASCI<sup>33–35</sup> and DMRG<sup>36–38</sup> approaches, both for ground state calculations and as approximate solvers in CASSCF<sup>39–42</sup> orbital optimizations within large active spaces. ASCI and DMRG are complementary methods to treat strong correlation in many-body systems, based on different heuristics: the former finds the most relevant Slater determinants for a truncated ground state description exploiting perturbative estimates iteratively, whereas the latter leverages the simple orbital entanglement structure in ground state wave functions to determine a compact Matrix Product State (MPS) wave function expansion.<sup>37</sup>

Here, we briefly outline the two methods, and refer the reader to the relevant literature and the [Supporting Information](#) (SI) for further details. Additionally, we present a new flavor of ASCI to target pure spin states, based on organizing the Slater determinants in Configuration State Function (CSF) families. This approach, which we label SP-ASCI, is necessary to avoid spin contamination in the truncated wave functions for the iron–sulfur clusters.

**2.1. ASCI and ASCI-SCF.** The ASCI approach relies on an efficient Selected Configuration Interaction (SCI) protocol to describe ground states. Using an iterative approach based on perturbative estimations,<sup>43–45</sup> ASCI can identify the determi-

nants in the Hilbert space that have large coefficients in the ground state wave function. Truncating the full Hilbert space to this determinant subset and subsequently projecting the Hamiltonian operator, results in highly compact approximate wave functions, which can nonetheless capture the static correlation of many-body systems accurately. This typically requires an active space formulation, and hence, ASCI is successful in describing multireference systems with a limited number (i.e., less than 50) of correlated orbitals. Dynamical correlation within the active space can be recovered perturbatively,<sup>34</sup> and ASCI has been shown to provide near FCI accuracy for the ground state energies and spectral functions for a wide variety of challenging, strongly correlated molecular and extended systems.<sup>33–35,41,46–50</sup> As is usual in SCI approaches, the orbital basis chosen to define the Hamiltonian has a critical effect on the convergence of ASCI, and simple choices, such as the natural orbital basis,<sup>51–54</sup> do not always ensure rapid convergence. It is for this purpose that the more sophisticated CASSCF orbital optimization can provide a decisive advantage, since it determines the variationally optimal orbital basis for a multireference wave function. Using ASCI in conjunction with CASSCF has been shown to enable the study of large active spaces in transition metal systems,<sup>41,55</sup> and for this reason, we have chosen to employ this method for the study of the iron–sulfur clusters.

**2.2. Spin Pure ASCI Mimicking CSFs.** While ASCI has been shown to successfully propose highly accurate ground state truncations, being a SCI approach it is susceptible to breaking symmetries. This happens when the generator of the symmetry  $O$  and the Hamiltonian  $H$  do not commute after being projected to the ASCI truncation. For (nonrelativistic) systems with strong magnetic character, such as the iron–sulfur clusters in this work, the breaking of spin symmetry (i.e.,  $O = S_{\text{tot}}^2$ ) can become a major computational problem, and we did indeed observe a large degree of spin contamination using ASCI even for modest active spaces in these systems. This difficulty arises from the fact that the iterative search for an optimal truncation in ASCI is formulated in terms of single Slater determinants, which are not generally eigenstates of the total spin operator. A way to avoid spin symmetry breaking is hence to express the Hilbert space truncation in terms of linear combinations of Slater determinants with definite spin state, so-called Configuration State Functions (CSF).<sup>39</sup> In this spirit, here, we build the ASCI truncation in terms of groups of determinants which we refer to as *CSF families*: These correspond to all possible determinants with a specified occupation scheme, defined by which orbitals are empty, singly and doubly occupied. Defined this way, the CSF families span all CSFs of a particular orbital occupation, and the ASCI truncation is guaranteed to preserve spin symmetry. Not all CSFs in a CSF family have the same spin quantum number, and we, further, select eigenstates with the smallest possible spin quantum number by adding a spin penalty term  $\lambda S_{\text{tot}}^2$  to the Hamiltonian during the energy calculation. This novel ASCI implementation leveraging an expansion in CSF families and spin penalization, which we label spin pure ASCI (SP-ASCI), enables treating targeted spin states in strongly correlated systems accurately, as we show in the [Results](#) section. We refer to the [SI](#) for details on the implementation and a discussion with related existing methods to resolve spin contamination in SCI-related electronic structure algorithms.<sup>56–58</sup>

**2.3. DMRG and DMRG-SCF.** DMRG is a very powerful approach suitable for the treatment of strongly correlated systems that was originally developed in solid state physics.<sup>36,59</sup> It has been established as one of the reference methods for the electronic structure calculations of strongly correlated molecules requiring very large active spaces.<sup>38,60–63</sup> Complexes with multiple transition metal centers are, because of the large quasi-degeneracy of *d* shells, typical examples of such species and belong to the most advanced quantum chemical applications of DMRG.<sup>26,42,64–66</sup>

The DMRG method is a variational procedure, which optimizes the wave function in the form of MPS.<sup>37</sup> The practical version of DMRG is the two-site algorithm, which provides the wave function in the two-site MPS form

$$|\Psi_{\text{MPS}}\rangle = \sum_{\{\alpha\}} \mathbf{A}^{\alpha_1} \mathbf{A}^{\alpha_2} \dots \mathbf{W}^{\alpha_i \alpha_{i+1}} \dots \mathbf{A}^{\alpha_n} |\alpha_1 \alpha_2 \dots \alpha_n\rangle \quad (1)$$

where  $\alpha_i \in \{|0\rangle, |\downarrow\rangle, |\uparrow\rangle, |\downarrow\uparrow\rangle\}$  for a given pair of adjacent indices  $[i, (i + 1)]$ ,  $\mathbf{W}$  is a four index tensor, which corresponds to the eigenfunction of the electronic Hamiltonian expanded in the tensor product space of four tensor spaces defined on an ordered orbital chain, so-called *left block* ( $M_l$  dimensional tensor space), *left site* (four dimensional tensor space of *i*th orbital), *right site* (four dimensional tensor space of  $(i + 1)$ th orbital), and *right block* ( $M_r$  dimensional tensor space). The MPS matrices  $\mathbf{A}$  are obtained by successive application of the singular value decomposition (SVD) with truncation on the  $\mathbf{W}$ 's and iterative optimization by going through the ordered orbital chain from *left* to *right* and then sweeping back and forth.<sup>61</sup> The maximum dimension of MPS matrices which is required for a given accuracy, so-called bond dimension [ $M_{\text{max}} = \max(M_l, M_r)$ ], can be regarded as a function of the level of entanglement in the studied system.<sup>67</sup> Among others,  $M_{\text{max}}$  strongly depends on the order of orbitals along the one-dimensional chain<sup>68,69</sup> as well as their type.<sup>70–72</sup>

Similarly to ASCI, DMRG can replace the exact diagonalization in the CASSCF procedure, which leads to the formulation of the method usually denoted as DMRG-SCF.<sup>73,74</sup> Since different elements of the two-particle reduced density matrices (2-RDMs) are collected at different iterations of the DMRG sweep,<sup>75</sup> the one-site DMRG algorithm has to be used for the final computations of the 2-RDMs to ensure the same accuracy of all their elements.<sup>73</sup>

As was mentioned above, the studied systems are prone to spin contamination. There exist spin-adapted formulations of quantum chemical DMRG;<sup>76–78</sup> however since the spin-adapted version of the MOLMPS program,<sup>42</sup> which was used in the current study, is under development, we used an approach similar to the one described in the previous section. In particular, we penalized higher spin states of the given spin projection by an additional term added to the Hamiltonian ( $\lambda S_{\text{tot}}^2$ ).

### 3. METHODOLOGICAL DETAILS

In this study, we consider the  $[\text{Fe}_4\text{S}_4(\text{SMe})_4]^{-2}$  clusters, with  $\text{Me} = \text{CH}_3$ , which correspond to a family of comparatively simple model systems of experimental and theoretical interest, since they serve as approximate structural motifs of the complex iron based catalytic centers in biologically relevant enzymes.<sup>26,79–83</sup> Formally, the  $-2$  charge corresponds to an average oxidation number of  $+2.5$ , which can be interpreted as two pairs of Fe(II) and Fe(III) atoms. To study the effect of

cluster geometry on the energy and spin ordering, we performed broken-symmetry (BS) DFT geometry optimizations for different spin states of this cluster, using the TPSSh functional and a mixed aug-cc-pVDZ (Fe, S) and cc-pVDZ (H,C) basis set, which we denote as (aug)-cc-pVDZ. This basis set has 568 basis functions. We determined 3 geometries, labeled 2A, 2B, and 2C. Geometry 2A was obtained by optimizing the high spin  $2S + 1 = 19$  state, corresponding to the maximal number of Fe-*d* electrons for the considered oxidation number being unpaired and having parallel spin. Both geometries 2B and 2C were obtained by optimizing the spin singlet. These correspond to distinct minima of the geometry optimization, energetically equivalent within chemical accuracy at the mean field level, but differing by the relative positions of the  $\text{Fe}^{2+}$  and  $\text{Fe}^{3+}$  atoms. We show a sample geometry (2A) in Figure 1 and refer to the SI for the .xyz files

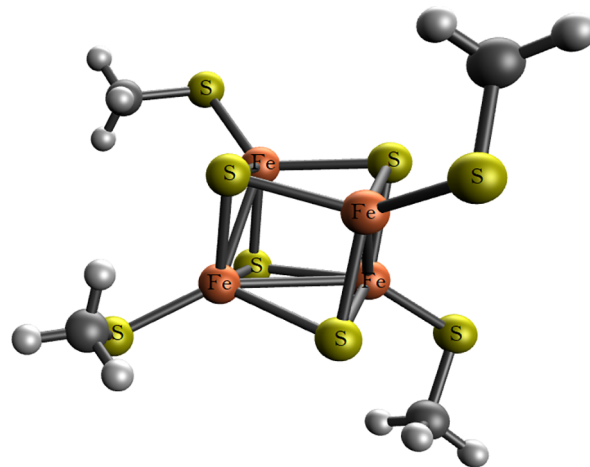


Figure 1. Sample geometry 2A for the  $[\text{Fe}_4\text{S}_4(\text{SMe})_4]^{-2}$  clusters.

Table 1. Summary Table Relating the  $[\text{Fe}_4\text{S}_4(\text{SMe})_4]^{-2}$  Cluster Labels to Their Geometries<sup>a</sup>

cluster	2S + 1	BS-DFT	HS-ROHF (2S + 1)
2A (Fe <sub>4</sub> )	19	−8401.048191	−8389.083540 (19)
2B (Fe <sub>4</sub> )	1	−8401.092653	−8389.026178 (19)
2C (Fe <sub>4</sub> )	1	−8401.092522	−8389.024431 (19)
2R <sup>26</sup> (Fe <sub>4</sub> )			−8388.979087 (19)

<sup>a</sup>Each geometry was obtained by performing a BS-DFT optimization with different target spin states  $2S + 1$ . We considered three geometries. The BS-DFT calculations used a mixed aug-cc-pVDZ (Fe, S) cc-pVDZ (C, H) basis set and the TPSSh functional. We also include the geometry in ref 26 in our study as reference. We, further, list the ROHF energies for the high spin (HS,  $2S + 1 = 19$ ) states in each cluster geometry, which we localized and used as the starting point for the CASSCF orbital optimizations.

containing the Cartesian coordinates. In Table 1, we provide the summary of the cluster labels and spin states, together with the BS-DFT energies. To provide a transparent comparison with previous studies, we also used the geometry in ref 26, which we label here as 2R. In the SI, we further include the ROHF and CASSCF energies for 5 geometries of the  $[\text{Fe}_3\text{S}_4(\text{SMe})_3]^{-2}$  clusters, which we used as test systems to benchmark our algorithms, as well as similar results for the 2R

geometry with the def2-SVP basis set, to offer a direct comparison with the results reported in ref 26.

For each cluster geometry  $[\text{Fe}_4\text{S}_4(\text{SMe})_4]^{-2}$  and spin state, we optimized its orbitals using the following protocol: First, we performed a Restricted Open-Shell Hartree–Fock (ROHF) calculation on a high-spin (HS) state, namely,  $2S + 1 = 19$ . We report the HS-ROHF energies, obtained with the (aug)-cc-pVDZ basis set, in the last column of Table 1. Already at the mean-field level, we can observe a huge effect on the energy due to slight geometry variations. In particular, we note that, with the mixed (aug)-cc-pVDZ basis set, the reference geometry 2R is not optimal for the oxidation state considered here, and that the 2A geometry, optimized for the high spin state, is the most stable at the ROHF level. Further details regarding the ROHF starting points can be found in the SI.

Those ROHF orbitals then serve as starting points for CASSCF orbital optimizations. For most of our calculations, we used a (54e, 36o) active space, including 20 ( $5 \times 4$ ) Fe-3d, 12 ( $3 \times 4$ ) bridge S-3p orbitals, and the four ( $1 \times 4$ ) ligand S-3p orbitals that point into the corresponding Fe atom. To simplify the active space identification, we performed a Pipek–Mezey<sup>84</sup> orbital localization of the core and valence orbitals separately, as has been done in previous studies of these systems to define the same active space.<sup>26</sup> Despite the fact that neither the ROHF, nor the ASCI and DMRG energies are invariant under such localization (due to mixing of open- and closed-shells), it is advantageous for the post-HF processing since it allows us to choose chemically motivated active spaces easily, it improves the CASSCF convergence, and further simplifies the interpretation of correlation functions.

Whether CASSCF captures the correct physical behavior can be active space dependent, especially in strongly correlated systems such as iron-based clusters.<sup>41</sup> Therefore, we study the effect of the active space choice in the  $[\text{Fe}_4\text{S}_4(\text{SMe})_4]^{-2}$  clusters, considering active spaces of increasing size.

- (22e, 20o): This is a minimal active space, containing exclusively the 20 ( $5 \times 4$ ) Fe-3d orbitals and electrons. While the Fe electrons are likely the main actors in the catalytic properties of the cluster, this active space does not account explicitly for charge or spin fluctuations between the iron and sulfur centers and, thus, can only account implicitly for the double-exchange mechanism, which typically governs the magnetic correlations in transition metal clusters of mixed oxidation number.<sup>85</sup> Still, recent studies<sup>58</sup> have shown that this type of minimal active space may be enough to capture energy gaps, and thus, we include it in our study. It further offers an important point of reference to infer the role of the additional orbitals included in the subsequent active spaces.
- (46e, 32o): This active space includes the 20 ( $5 \times 4$ ) Fe-3d orbitals and further the 12 ( $3 \times 4$ ) S-3p orbitals of the four bridging S atoms. Thus, it is the minimal active space to explicitly account for double-exchange interactions, missing an explicit treatment of the ligand sulfur orbitals.
- (54e, 36o): This active space further includes the four ( $1 \times 4$ ) S-3p orbitals from the ligand S atoms pointing toward their bonded Fe center. This is the same active space considered in ref 26 and accounts for ligand effects into the iron–sulfur cluster. Given the relatively small size of the cluster, including only four Fe centers, these

ligand effects are likely to be important for a quantitative description of the system, and they are known experimentally to change photoemission spectra appreciably in the valence region of iron–sulfur cubanes.<sup>81,82</sup>

- (86e, 52o): The largest active space we considered enhances the (54e, 36o) one by adding the 12 ( $3 \times 4$ ) Fe-3p, as well as the four ( $1 \times 4$ ) Fe-3s orbitals. Although chemical intuition may suggest that an explicit treatment of these orbitals in the active space should be unnecessary, our results below indicate that including them helps unbiased the CASSCF optimization process, as well as accounting for a sizable contribution to the correlation energy.

In this work, we study of the effect of active space choice in the total energy as a function of spin state, the relative spin energy gaps, charge densities, as well as the magnetic structure of the cluster on the example of the 2A geometry.

We used SP-ASCI as the CAS solver approximation in these active spaces. Following the suggestions in ref 41, we performed a stepwise orbital optimization, performing sequential ASCI-SCF calculations in which we systematically increase the number of determinants in the solver, starting with  $10^5$  determinants, and increasing as  $2.5 \times 10^5$ ,  $10^6$ ,  $2 \times 10^6$ , and  $5 \times 10^6$ . In terms of CSF families, this sequence corresponds for the (52e, 36o) active space to approximately 4, 20, 50, 100, and 230 CSF families, respectively. Although the first two optimizations contain a small number of CSF families, we have observed that we reach lower energies by starting there, as opposed to starting the CASSCF optimization from the ROHF orbitals directly with a  $10^6$  ASCI-SCF calculation. This may point to some effective preoptimization of the inactive orbitals.

While the union of the CSF families contains as many CSFs as Slater determinants, not all CSFs in the families have the spin of interest. For example, the CSF family consisting of two singly occupied orbitals, with one electron of spin up and one electron of spin down, has two CSFs (and two Slater determinants): one of the CSFs corresponds to a spin singlet, the other to a spin triplet. Hence, when interested in a particular spin state, a given CSF family has less relevant CSFs than the total number of Slater determinants, leading to expansions in CSFs being more compact than in terms of Slater determinants.<sup>39</sup> Thus, to assess the variational flexibility of our SP-ASCI method, it is necessary to transform from the number of Slater determinants to the number of CSFs of right spin. Since we are always after the lowest possible spin for a given spin-z quantum number [this means a singlet when there are the same number of electrons of spin up and down  $N_{e,\uparrow} = N_{e,\downarrow}$ , a triplet when  $N_{e,\uparrow} = N_{e,\downarrow} + 2$ , etc.], we can relate the number of CSFs of right spin  $N_{M=S}^{\text{CSF}}$  in a given family to the corresponding number of determinants  $N^d$  as (see Chapter 2 in ref 39)

$$\frac{N_{M=S}^{\text{CSF}}}{N^d} = \frac{2S + 1}{S_{\text{max}} + S + 1} \quad (2)$$

where  $S_{\text{max}}$  is the maximal spin possible in the spin family. For the FeS clusters and active spaces considered in this work, where the maximal possible spin is  $2S_{\text{max}} + 1 = 19$ , this means that in our singlet calculations the number of singlet CSFs corresponds approximately to 10% of the total number of determinants. Therefore, in the largest SP-ASCI calculations, including  $\sim 5 \times 10^6$  determinants and  $\sim 230$  CSF families, we include  $\sim 5 \times 10^5$  singlet CSFs. For quintet calculations, this

increases to  $\sim 2 \times 10^6$  CSFs. A comprehensive table presenting the number of determinants, CSF families, and CSFs of right spin for the largest SP-ASCI calculations in the different geometries, active spaces, and spin states is provided in the SI.

The CASSCF optimizations performed in this work are highly complex, prone to falling into local minima. This becomes particularly apparent when comparing the CASSCF energies for different spin states of the same geometry, which often would show gaps of several mHa, in extreme cases even  $>10$  mHa. In these cases, following the suggestions in ref 41, we attempt to escape the local minima of, for example, spin state  $S$  by restarting its CASSCF with the optimized orbitals of spin state  $S \pm 1$ . Alternatively, within the SP-ASCI framework, we can restart the CASSCF with orbitals obtained from a low determinant ASCI-SCF without imposing the total-spin conservation symmetry, introducing spin contamination but potentially escaping local minima. Restarting the optimization again, recovering the spin conservation, can then result in lower energies if a better minimum is found. We continue this process until the CASSCF energy converges within 1 mHa. It is important to note that this strategy does not guarantee reaching the global minimum during the CASSCF optimization, and instead, the results correspond just to stable local minima. This is unavoidable in complex nonlinear optimizations as the ones pursued here, involving 584 basis functions and large active spaces. Still, obtaining physical magnitudes, such as spin gaps and correlation functions, in good agreement with the theoretical and experimental literature gives us confidence that our results are representative of the actual chemistry of these clusters.

To obtain an estimate of the FCI energy within the active spaces, we performed ASCI+PT2 extrapolations<sup>34</sup> with the optimized CASSCF orbitals. For this, we computed ASCI+PT2 energies for truncations of  $5 \times 10^5$ ,  $10^6$ ,  $2 \times 10^6$ ,  $5 \times 10^6$  determinants (and up to  $7 \times 10^6$  determinants for the largest active space calculations), and then fit the ASCI+PT2 energy versus the PT2 correction as a straight line. The value for the fitted  $y$  intercept corresponds to our best estimate for the energy with no perturbative correction, that is, the FCI limit. This is a common practice for selected configuration interaction approaches.<sup>50,86,87</sup> We report the uncertainty of the  $y$  intercept as a measure of the systematic error of the extrapolation. Notably, this extrapolation is less straightforward for the Fe–S cubanes than for smaller systems previously studied with ASCI, since the ASCI+PT2 energies do not follow a perfect linear dependency as a function of the PT2 correction. Additionally, the adequacy of the linear fit can depend on the system studied. In particular in this work, geometry 2C observed a noticeably larger deviation than the other geometries, resulting in larger uncertainty in the extrapolated energies because of the dismissal of outliers in the fit (see caption in Table 3). Despite this inconveniences, the perturbative extrapolation offers a viable estimate of the missing dynamical correlation in the ASCI wave function with quantifiable fit error.

Given the inherent complexity of the electronic structure in FeS clusters, we subsequently investigate them with DMRG, which as discussed above is based on a different heuristic than ASCI. We use the CASSCF orbitals optimized by ASCI as starting points for further CASSCF orbital optimization, this time using the DMRG approach as a solver and bond dimensions  $M = 2000$ . In the case of DMRG-SCF, active-orbital rotations were not considered, while these do

enter in the ASCI-SCF optimization, see SI. Once this subsequent approximation is converged, we performed accurate DMRG calculations with the dynamical block state selection (DBSS)<sup>68</sup> and predefined truncation error  $TRE = 10^{-6}$  (unless otherwise stated, depending on the structure and spin state, this corresponds up to  $M = 16\,000$ ). As far as computational complexity is concerned, our implementation of both DMRG and ASCI methodologies have similar timings.

Our correlated CAS calculations on different geometries and spin states provide an improved description of the tunability of the magnetic and electronic properties of Fe–S cubanes with respect to single-reference methodologies, such as mean-field theory or BS-DFT. Further, as mentioned in the introduction, the optimized single-particle orbitals obtained from the MCSCF self-consistency can serve as starting point for fully correlated studies of these systems, recovering the dynamical correlation beyond the active space, which in this study we neglect within the CASSCF variational Ansatz. The complexity of such calculations puts them however well beyond the scope of this paper. Hence, rather than the highest accuracy to sub mHa (meV) level, we strive to a consistent description to chemical accuracy, that is,  $\sim 2$  mHa. The use of two complementary solvers allows us to increase the confidence in the reliability of our results within this precision, reducing the bias in our physical conclusions, and validating the different approximations inherent to both approaches.

Finally, we note that we performed additional calculations on some of the clusters to better illustrate our conclusions. For instance, we performed ASCI-PT2 and DMRG calculations on the unoptimized, although localized, ROHF orbitals, in order to investigate the effect of the CASSCF optimization, as well as ASCI calculations on the high-spin state using the singlet CASSCF optimized orbitals to estimate total spin gaps. As discussed above, we also tested different active spaces for the 2A cluster and include a brief note on basis set choice in the SI.

The BS-DFT and ROHF calculations were performed in NWChem,<sup>88</sup> FCI-CASSCF (see SI) calculations were performed in MOLPRO,<sup>89,90</sup> ASCI-based calculations were performed with a modified version of QChem,<sup>91</sup> and the DMRG(-SCF) calculations were performed with the MOLMPS program<sup>42</sup> interfaced to ORCA.<sup>92,93</sup>

## 4. RESULTS

**4.1. Discussion of Geometries.** The cluster geometry plays a crucial role in the catalytic activity of iron–sulfur clusters, particularly considering the high tunability of the protein environment in which they are often embedded. For the cubane systems considered in this work, the relevant parameters describing the FeS “cube”, i.e., the Fe–S bond lengths, the Fe–Fe distances and the Fe–S–Fe angles, are equivalent to averages in crystallographic data for similar compounds.<sup>94,95</sup> These geometries are significantly different from an ideal cube. The average Fe–S–Fe angles are  $\sim 75^\circ$ , in very good agreement with the experimental values where the corresponding average angle is  $73.81^\circ$ ,<sup>94</sup> but significantly smaller than a right angle that is present in an ideal cube. Similarly, in a perfect cube, the average Fe–Fe distance would be exactly  $\sqrt{2}$  times the average Fe–S bond length. However, our geometries show deviations of 12–16% from this ideal relation, consistent with the deviations of 15% in the experimental geometry. Besides the departure from the ideal cubic geometry, these clusters present a further asymmetry: within the Fe–Fe distances in a given cluster, there are always

two Fe-pairs with shorter distance than all other possible combinations. For geometries 2B, 2C, and 2R, this difference is only slight (the shorter Fe–Fe distances are  $\sim 3\%$  smaller), but geometry 2A has a more pronounced asymmetry with the shorter Fe–Fe distance being  $\sim 11\%$  smaller. As our results suggest, this subtle difference in the geometry has huge consequences to the electronic structure: it reduces the largest spin gap, that is, the energy difference between the most stable singlet and the  $2S + 1 = 19$  configurations, by a factor of 3! This is a remarkable manifestation of the electronic tunability of these catalytic centers as a result of small variations in the cube's geometry. The actual values for the Fe–Fe and Fe–S bond lengths, as well as the Fe–S–Fe angles, are tabulated in the SI.

Experimentally, in solid state, the geometries of derivatives of the present calculated compounds, that is,  $[\text{Fe}_4\text{S}_4(\text{SCH}_2\text{Ph})_4]^{2-}$  and  $[\text{Fe}_4\text{S}_4(\text{SPh})_4]^{2-}$  have been measured; the average Fe–Fe distances are  $2.747 \text{ \AA}^{94}$  and  $2.736 \text{ \AA}^{95}$  respectively, while the average Fe–S distance is  $2.286 \text{ \AA}$  for both anions. Comparing our calculated average Fe–Fe and Fe–S distances with these available crystallographic data, we found that our average calculated Fe–Fe distances of the 2A–2C structures are about 0.5–8% elongated, while our Fe–S distances are elongated about 2–4% with respect to the experimental data. These deviations are reasonable, given that the experimental data correspond to derivatives of our calculated  $[\text{Fe}_4\text{S}_4(\text{SMe})_4]^{2-}$  units in the solid state, and hence, we are confident that our geometries are representative of the actual FeS clusters in catalytic centers.

**4.2. ASCI and DMRG with Hartree–Fock Orbitals.** To assess the effect of the orbital optimization on the physical description of the iron–sulfur clusters, we first compute the energies for the low lying spin states with the unoptimized HS-ROHF orbitals, localized via the Pipek–Mezey scheme. We report the variational ASCI and DMRG energies in the (54e, 36o) active space for the  $\text{Fe}_4$  clusters in Table 2. To provide a comparison with the existing literature, we report the energies of the low lying spin states for the 2R geometry using the def2-SVP basis set in the SI.

We observe that the ASCI and DMRG energies in Table 2 follow the same hierarchy as the mean-field energies in Table 1, with 2A being the most stable geometry and 2R the least stable one. The DMRG energy gaps between consecutive spin states are nonetheless comparable between geometries, typically  $\sim 1 \text{ mHa}$ . Notice that the ASCI and DMRG energies in Table 2 are above the canonical ROHF energies in Table 1, which is due to the aforementioned localization of ROHF orbitals mixing open- and closed-shells. Further, inspecting the DMRG energies for the 2B and 2C geometry, we observe that the energetic degeneracy present at the mean field level (c.f., the BS-DFT and ROHF energies in Table 1) is lifted with this correlated description. Indeed, the singlet states of 2B and 2C are now split by an appreciable gap of  $\sim 5 \text{ mHa}$ , significantly larger than the gap between spin states in the same geometry.

We note that the ASCI+PT2 extrapolated energies in Table 2 show large gaps of tens of mHa between the different spin states, as well as comparably large extrapolation errors. These gaps are not consistent with either previous results in the literature,<sup>26</sup> or with our DMRG calculations in the right most column of Table 2, or indeed with the trends observed for the  $\text{Fe}_3$  clusters in the SI. Furthermore, the PT2 extrapolations in these systems are rather unreliable, since the perturbative corrections are quite large ( $>60 \text{ mHa}$ ), and the convergence

**Table 2. Extrapolated ASCI and DMRG Energies ( $E - 8380.0 \text{ Ha}$ ) for the (54e, 36o) active space of  $[\text{Fe}_4\text{S}_4(\text{SMe})_4]^{2-}$ , Using the High Spin ( $2S + 1 = 19$ ) ROHF Orbitals, Localized with Pipek–Mezey, with the (aug)-cc-pVDZ Basis<sup>a</sup>**

cluster geom.	$2S + 1$	ASCI+PT2 extrapol.	DMRG (TRE = $5 \times 10^{-6}$ )
2A	5	$-9.0202 \pm 0.0024$	$-9.011678$
	3	$-8.9580 \pm 0.0074$	$-9.011427$
	1	$-8.9645 \pm 0.0101$	$-9.012364$
2B	5	$-8.8975 \pm 0.0389$	$-8.989614$
	3	$-8.9448 \pm 0.0094$	$-8.990533$
	1	$-8.9054 \pm 0.0169$	$-8.991705$
2C	5	$-8.8685 \pm 0.0451$	$-8.985393$
	3	$-8.9010 \pm 0.0118$	$-8.986240$
	1	$-8.8751 \pm 0.0137$	$-8.987101$
2R	5	$-8.8772 \pm 0.0146$	$-8.928211$
	3	$-8.8828 \pm 0.0164$	$-8.929151$
	1	$-8.8484 \pm 0.0166$	$-8.930184$

<sup>a</sup>The ASCI-PT2 extrapolations to the FCI limit use a linear extrapolation from calculations with  $5 \times 10^5$ ,  $1 \times 10^6$ ,  $2 \times 10^6$ , and  $5 \times 10^6$  determinants. The error bars correspond to the standard deviation of the linear fit, and are thus just a measure of the extrapolation error alone. The DMRG energies for the 2R geometry used TRE =  $10^{-5}$ .

behavior is far from linear in several of the spin states and used geometries. Indeed, for the 2A, 2B, and 2C geometries we dismissed, as a clear outlier, the  $5 \times 10^5$  ASCI calculation in the extrapolation since it shows poor convergence toward the FCI limit. These issues are symptomatic of ASCI converging very slowly in the localized ROHF orbital basis. These convergence issues are not entirely surprising, since the number of CSFs we include is smaller than has been observed necessary in simpler systems in other selected CI implementations.<sup>96</sup> In a sense, this is a prize to pay for the current spin-pure implementation of ASCI: a penalty to the variational flexibility in order to keep spin symmetry unbroken. For smaller molecular systems, rotations to an approximate natural orbital basis drastically improve the ASCI convergence in terms of determinants. Unfortunately, these cubane clusters have a too pronounced multireference character in the localized ROHF basis, such that even at 5 million determinants the one-particle reduced density matrix (1-RDM) is not representative for the true ground state, and thus the corresponding natural orbital rotation does not resolve the convergence problem. Instead, a more sophisticated single-particle rotation is needed for ASCI to provide reliable results in these exceptionally complex systems, and thus we turn our attention to CASSCF orbital optimization. We will see that once we perform the orbital optimization, the ground state wave functions become much more compact, and SP-ASCI truncations of  $\sim 5$  million determinants provide an accurate description of these systems, in good agreement with DMRG.

**4.3. CASSCF with ASCI and DMRG.** The CASSCF energies for the low lying spin states for the four cluster geometries, employing SP-ASCI and DMRG as solvers with a (52e, 36o) active space, are summarized in Table 3. In the case of ASCI we report extrapolated energies to the FCI limit, complementing ASCI with second order perturbation theory.<sup>34</sup> For accurate DMRG calculations, we have used the tight truncation error criterion TRE =  $10^{-6}$ .

**Table 3. CASSCF and Extrapolated Energies ( $E - 8380.0$  Ha) using SP-ASCI and DMRG for the (54e, 36o) Active Space of  $[\text{Fe}_4\text{S}_4(\text{SMe})_4]^{-2}$ , Starting from the High Spin ( $2S + 1 = 19$ ) ROHF Orbitals, Localized with the Pipek–Mezey Scheme, with the (aug)-cc-pVDZ Basis<sup>a</sup>**

Cluster Geom.	2S + 1	CASSCF SP-ASCI-SCF	ASCI+PT2 extrapol. SP-ASCI	DMRG-SCF (M = 2000)	DMRG (TRE = 10 <sup>-6</sup> )
2A	5	-9.150451	-9.1553 ± 0.0010	-9.154563	-9.155436
	3	-9.150856	-9.1554 ± 0.0008	-9.155611	-9.155571
	1	-9.150950	-9.1554 ± 0.0007	-9.155072	-9.155582
2B	5	-9.117029	-9.1230 ± 0.0013	-9.124550	-9.126843
	3	-9.117290	-9.1239 ± 0.0009	-9.124132	-9.126312
	1	-9.117792	-9.1239 ± 0.0011	-9.122910	-9.126381
2C	5	-9.089257	-9.0953 ± 0.0010	-9.089034	-9.092818
	3	-9.088027	-9.0924 ± 0.0013	-9.088379	-9.091081
	1	-9.090888	-9.0967 ± 0.0017	-9.088452	-9.091410
2R	5	-9.063877	-9.0714 ± 0.0010	-9.073519	-9.074443
	3	-9.062709	-9.0690 ± 0.0010	-9.071405	-9.072118
	1	-9.063875	-9.0705 ± 0.0007	-9.069628	-9.072103

<sup>a</sup>For the CASSCF energies with ASCII, the results correspond to calculations with  $5 \times 10^6$  determinants. These are the final steps of a series of SP-ASCI-SCF calculations starting at  $1 \times 10^5$  determinants and progressively increasing the number of determinants to improve the orbitals sequentially. The ASCII+PT2 extrapolated results are estimating the FCI limit using a linear extrapolation from calculations with  $5 \times 10^5$ ,  $1 \times 10^6$ ,  $2 \times 10^6$ , and  $5 \times 10^6$  determinants, starting from the orbitals obtained from the SP-ASCI-SCF with  $5 \times 10^6$  determinants. The error bars correspond to the standard deviation of the linear fit, and are thus just a measure of the extrapolation error alone. The extrapolation for the 2C singlet state was performed considering only the last with 3 calculations.

The different geometries show minute energy gaps between subsequent spin states. We note the good agreement between ASCII and DMRG, which on average differ by just 2.2 mHa, that is, approximately chemical accuracy (1.6 mHa or 43.5 meV). This level of agreement between two methods relying on significantly distinct wave function Ansätze is a crucial validation for studying strongly correlated molecules of this complexity. Moreover, since DMRG has been validated as CASSCF solver against FCI (see  $\text{Fe}_3$  results in the SI), this agreement shows that ASCII plus perturbative correction also provides an accurate CAS approximation to use in the orbital optimization. [It is important to remember that this does not mean that we have reached a global minimum in the CASSCF optimization but that the DMRG-SCF optimization subsequent to ASCII-SCF did not find a better set of orbitals in these cases. We note that this is still a possible outcome, and in particular, we show an example of this situation in the SI for the def2-SVP basis set calculations in the 2R geometry.] Furthermore, the CASSCF optimized orbitals resolve the convergence issues that ASCII presents in the ROHF orbital basis, resulting in more reliable perturbative extrapolations, with errors of  $\sim 1$  mHa. We find, thus, that the orbital optimization greatly condenses the wave function expansion in terms of Slater determinants, making our  $\sim 5$  million determinant truncation comparatively accurate to DMRG.

For all geometries, we observe the singlet state to be the most stable at the variational CASSCF level, with the exception of the 2R geometry, in which the singlet and quintet are essentially degenerate. In general, the observed energy gaps are approximately 1 mHa or smaller. Upon extrapolation to the full CI limit with ASCII+PT2, the gaps remain small, and some degree of spin reordering is apparent. However, since in this case the gaps are of the order of magnitude of our extrapolation error, it is not possible to make any definitive statement about the actual spin orderings in the FCI limit. Achieving higher accuracy would be possible by increasing the number of determinants in ASCII, or the bond dimension in DMRG. However, the dynamical correlation beyond the active

space, neglected in this work, is likely to have a larger effect on the spin ordering. Hence, we refrain from further refining our CAS calculations in this regard, as our current accuracy suffices to provide for a reliable, orbital-optimized starting point for subsequent studies.

In contrast to the spin ordering, it is possible to make stronger claims about the largest spin gap in the systems, that is, the gap between the lowest ( $2S + 1 = 1$ ) and largest ( $2S + 1 = 19$ ) spin states. We summarize such gaps for the different geometries in Table 4, in which we compute the high spin

**Table 4. SP-ASCI Energies ( $E - 8380.0$  Ha), Plus PT2 Corrections, of the High Spin State  $2S + 1 = 19$  for the Different  $[\text{Fe}_4\text{S}_4(\text{SMe})_4]^{-2}$  Cluster Geometries in the (54e, 36o) Active Space with (aug)-cc-pVDZ Basis<sup>a</sup>**

geometry	2S + 1 = 19 energy [Ha] SP-ASCI (PT2)	variational gap [meV]	extrapolated gap [meV]
2A	-9.149945 (-0.000020)	-27.2	-149.7 (-95.2)
2B	-9.108935 (-0.000012)	-242.2	-408.2 (-487.1)
2C	-9.081856 (-0.000018)	-244.9	-405.4 (-462.6)
2R	-9.054036 (-0.000014)	-266.7	-449.0 (-503.4)

<sup>a</sup>The energies are computed using the CASSCF orbitals optimized for the singlet state. The last two columns report the spin gap in meV between the high spin and singlet states, computed as  $E_0^{2S+1=1} - E_0^{2S+1=19}$ , where the corresponding singlet energies were taken from Table 3. We report variational spin gaps, as well as extrapolated spin gaps including the PT2 correction. The numbers in parentheses are the spin gaps computed in the localized ROHF basis using DMRG.

energies with ASCII using the CASSCF optimized orbitals for the corresponding singlet state. This is likely a minor approximation in these systems, since we have observed that performing the CASSCF optimization on the high spin states explicitly only lowered the energy by  $\sim 1$ – $2$  mHa. We, further, report in parentheses the equivalent gaps computed in the localized ROHF basis with DMRG. While the high-spin state is generally higher in energy, we observe a strong geometry dependence for this gap, in several cases well resolved with the

accuracy of our methods. In particular, the 2A geometry presents the smallest extrapolated gap, of only  $\sim 150$  meV ( $\sim 5.5$  mHa), approximately three times smaller than the gap for the other geometries. This is significant, since geometry 2A was optimized for the high spin state, resulting in a more pronounced asymmetry in the Fe–Fe bonds discussed in section 4.1. While these trends can be observed in both the localized ROHF and optimized CASSCF orbital bases, the orbital optimization reduces the gaps appreciably for all but the 2A geometry.

Comparing the CASSCF results in Table 3 with the DMRG energies in the ROHF basis from Table 2, we note a significant energy stabilization. Indeed, in the 2R geometry we observe over 100 mHa energy difference between the results before and after the CASSCF optimization. Including the bridging and ligand S-3p orbitals is capturing a relevant component of the correlation energy, supported by the double-exchange picture<sup>97–99</sup> which is used to motivate the spin structure in these clusters. Below we study the correlation energy as a function of the active space size, which will further strengthen this interpretation. The effective energy gap between the reference geometry 2R and geometries 2A–2C increases upon orbital optimization, while the gaps between spin states are similar for both ROHF and optimized CASSCF orbitals. Moreover, the gap between the 2B and 2C singlet states increases significantly upon CASSCF optimization, from  $\sim 5$  mHa using localized ROHF orbitals and DMRG (see Table 2) to  $\sim 35$  mHa with the optimized CASSCF orbitals (see Table 3). This underlines the importance of the orbital optimization to accurately describe the electronic structure of these complicated clusters. Further, this huge energy gap resulting from the slight geometry differences between 2B and 2C, as well as the spin gaps shown in Table 4, highlight the exceptional geometry dependence of the electronic properties of these clusters, which underlies the catalytic tunability and prowess of FeS complexes. Given the size of the singlet-to-high-spin gaps in Table 6, as well as the energy gaps between different geometries, it is reasonable to expect that our conclusions will still apply after recovering dynamical correlation beyond the active space.

Beyond just considering the energetics, it is interesting to investigate the change of character of the active space orbitals upon the CASSCF optimization. In Figure 2 we show sample orbitals before and after the CASSCF optimization for the 2A geometry, and  $2S + 1 = 1$  spin state. We observe that there are still 20 orbitals of essentially exclusive Fe-3d character, compare, the two lower left panel in Figure 2. However, these present at times some degree of pairing into Fe-dimers. By this we mean that some of these orbitals are linear combinations of Fe-3d localized on two Fe centers. For instance, note how in the lower left panel of Figure 2, besides a dominant Fe-3d contribution in one of the four iron centers, there is a minor yet significant Fe-3d contribution from another iron center, bridged by the connecting S-3p orbitals. Further, for geometries where this pairing is strongly present, it defines two clear pairs, that is, we only observe pairing between Fe-3d orbitals in Fe atom pairs 1–2 and 3–4, but never between 3 and 1 or 3 and 2. These pairs coincide with the shortest Fe–Fe distances in the corresponding geometry, compare section 4.1.

This is a noteworthy phenomenon, since it is consistent with the magnetic structure expected for the low spin states of these systems: two high-spin Fe-dimers antiferromagnetically

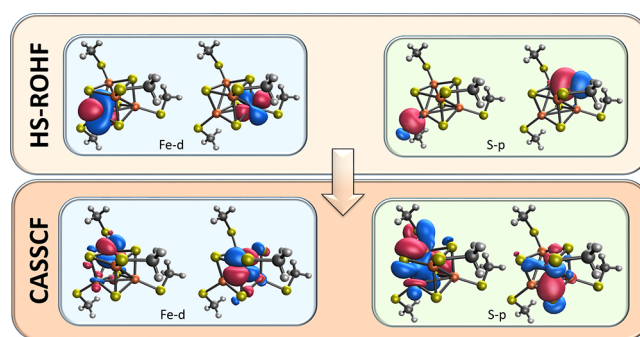


**Figure 2.** Sample orbitals before (HS-ROHF) and after the CASSCF rotation, for the 2A  $[\text{Fe}_4\text{S}_4(\text{SMe})_4]^{2-}$  cluster geometry, spin state  $2S + 1 = 1$ . The CASSCF results correspond to the final optimization, using the SP-ASCI solver with  $5 \times 10^6$  determinants. For the localized HS-ROHF, we show two orbitals from the Fe-3d set and 2 orbitals from the S-3p set. For the CASSCF calculation, we select two orbitals each of the same sections of the active space, which present significant changes with respect to the localized HS-ROHF orbitals.

coupled to result in an overall singlet state. Still, single-particle orbitals are not physically well-defined magnitudes. Thus, we confirm this picture by computing actual observables, such as spin–spin correlation functions  $C_{a,b}^S = \langle \hat{S}_a \times \hat{S}_b \rangle_0$ , accessible through the 2-RDM, where  $a$  and  $b$  denote single-particle orbitals and  $\langle \cdot \rangle_0$  denotes a ground state expectation value. From these correlation functions, we can evaluate effective spin multiplicities for the 3d-orbitals of the two Fe-dimers present in each  $[\text{Fe}_4\text{S}_4(\text{SMe})_4]^{2-}$  cluster. These effective multiplicities are shown in the upper panels of Figure 3, with two triangle markers of different orientation corresponding to each one of the two dimers in each geometry. The 2-RDM's were computed from the CASSCF optimized SP-ASCI wave functions with 5 million determinants. The left panels show effective multiplicities in the CASSCF orbital basis, the right

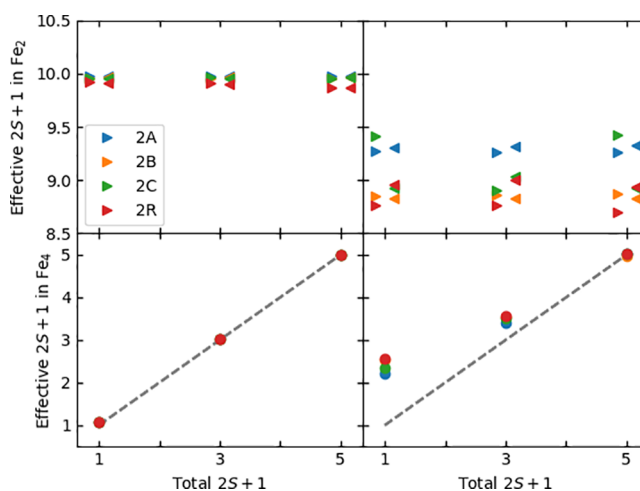


**Figure 3.** Effective spin multiplicity  $2S + 1$  for different subsets of Fe-3d orbitals from the CASSCF optimized SP-ASCI wave functions of the four cluster geometries with the (aug)-cc-pVDZ basis set and the (54e, 36o) active space. Upper panels: Multiplicities considering the Fe-3d orbitals of the two ferromagnetically coupled Fe-dimers within the  $[\text{Fe}_4\text{S}_4(\text{SMe})_4]^{2-}$  cluster. The left panel is computed in the CASSCF basis, the right panel is rotated to the localized ROHF basis. Lower panels: Multiplicities considering the Fe-3d orbitals of all four Fe atoms, in the CASSCF basis (left) and rotated to the localized ROHF basis (right). See text for details.

panels in the localized ROHF orbital basis (i.e., the 2-RDM was rotated back to the localized ROHF basis). In the CASSCF orbital basis (left panels), we observe high and equal effective multiplicities of  $2S_{\text{eff}} + 1 = 10$  for all Fe-dimers in all geometries and all total spin states. This corresponds, in its simplest interpretation, to 9 unpaired electrons of parallel spin. Each dimer is composed of two ferromagnetically coupled Fe atoms. Since this is independent of the total spin state of the cluster, that is, the Fe-dimers are high-spin for all singlet, triplet and quintet, this suggests a weak ligand field splitting for the 3d-orbitals of the Fe-centers, as well as a dominant double-exchange mechanism producing ferromagnetic order. When considering then the effective multiplicity due to the 3d-orbitals of all four Fe atoms (lower panels in Figure 3), we see that in the CASSCF orbital basis (left panel) the Fe-3d orbitals account for the full cluster spin, showing that the high-spin Fe-dimers couples antiferromagnetically with different relative orientations to give the total spin states. Rotating the 2-RDMs to the localized ROHF basis, and recomputing the effective dimer and  $[\text{Fe}_4\text{S}_4(\text{SMe})_4]^{-2}$  multiplicities in terms of the localized Fe-3d orbitals, the picture changes slightly, see right panels in Figure 3. Here, the Fe-dimers have a slightly reduced effective multiplicity, though still possessing a high-spin indicative of ferromagnetic correlation, and the full Fe-3d orbital manifold does not account for the total spin state of the cubane cluster. These changes suggest the presence of spin fluctuations from the Fe-3d orbitals into the rest of the system, likely the S-3p orbitals.

We can also observe similar fluctuations between the Fe-3d and S-3p orbitals in the orbital charge density, by examining the diagonal terms of the 1-RDM. In the lower panel of Figure 4, we show the orbital charge densities for the Fe-3s/3p, as well as valence S-3p and Fe-3d orbitals for the 2A cluster geometry, singlet state. These correspond to the diagonal 1-RDM components, rotated back to the localized ROHF basis. The orbital charge densities in the optimized CASSCF molecular orbitals are shown in the upper panel of the same figure. As the figure shows, there is clear charge density fluctuations from the localized Fe-3d orbitals into the S-3p.

To further support the double-exchange mechanism, we have studied pairwise orbital correlations by means of the mutual information.<sup>61</sup> Since the mutual information is a two-orbital (rather than a two-electron) quantity, it includes certain elements of 4-point correlation functions (i.e., ground state expectation values including up to four pairs of creation/annihilation operators).<sup>100</sup> We considered Fe-3d orbitals grouped by Fe-atom, as well as S-3p orbitals grouped by S atom, and show the mutual information between these groups in Figure 5. We show the mutual information between these groups from the 2A DMRG singlet wave function in the ROHF localized basis, using the (54e, 36o) active space in the left panel. We observe clear signatures of correlation between the Fe1–Fe4 and Fe2–Fe3 dimers, which correspond to the ferromagnetically pairs identified with the spin–spin correlation functions in Figure 3. We further observe some minor, though noticeable degree of correlation between the Fe-3d and bridge S-3p (S1–S4) orbitals, while the ligand S-3p (S5–S8) orbitals have weaker correlation to the Fe-3d's. The right panel of Figure 5 shows the difference between this mutual information computed in the (54e, 36o) active space, and the mutual information from a (22e, 20o) active space calculation. This active space does not include the S-orbitals, and thus there is no correlation between them and the Fe-3d's.

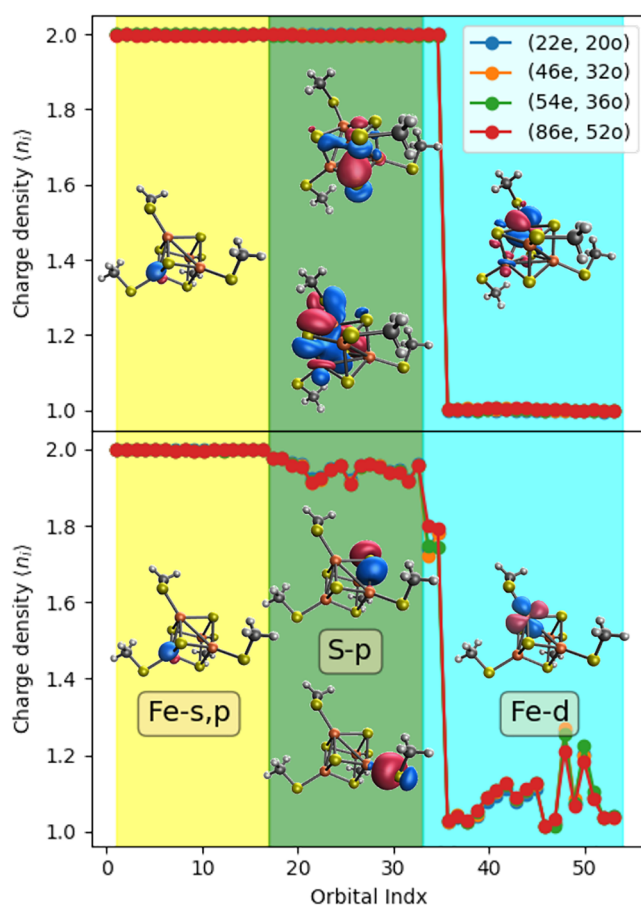


**Figure 4.** Upper panel: Orbital charge densities in the CASSCF wave function for the 2A geometry of the  $[\text{Fe}_4\text{S}_4(\text{SMe})_4]^{-2}$  cluster,  $2S + 1 = 1$ , for different active spaces in the optimized orbital basis. The wave function is computed with SP-ASCI, and  $5 \times 10^6$  determinants. We label the orbitals by their character before the optimization, that is, the labels correspond to the original active space order fed into the CASSCF routine. Lower panel: Same orbital charge densities of same wave function, in the localized ROHF basis. See text for details.

The difference figure thus reveals the effect of the S-3p orbitals in the Fe–Fe orbital correlations. We observe that including the S-3p orbitals explicitly changes the Fe–Fe correlations significantly. In particular, it is interesting to note that the correction to the dimer Fe1–Fe4 and Fe2–Fe3 correlations have opposite signs. Since the resulting mutual information (see right panel) are comparable for both panels, this may be the consequence of asymmetries in the localized ROHF basis. This analysis of mutual information, as well as the previous discussion in terms of spin–spin correlation functions and charge densities, is in perfect agreement with the magnetic structure expected for these clusters, and further with an underlying double-exchange interaction between Fe atoms, mediated by S electrons.

Beyond the Fe-3d pairing, the majority of the remaining active space orbitals show mixed character between bridge S-3p orbitals and Fe-3d, further supporting the double-exchange picture, c.f. lower right panel of Figure 2. Observing both these features, Fe-3d/Fe-3d pairing and Fe-3d/S-3p bridging, emerging from the CASSCF optimization is an important indicative that the optimized orbitals are a fundamentally better basis to describe the electronic properties of the iron–sulfur clusters.

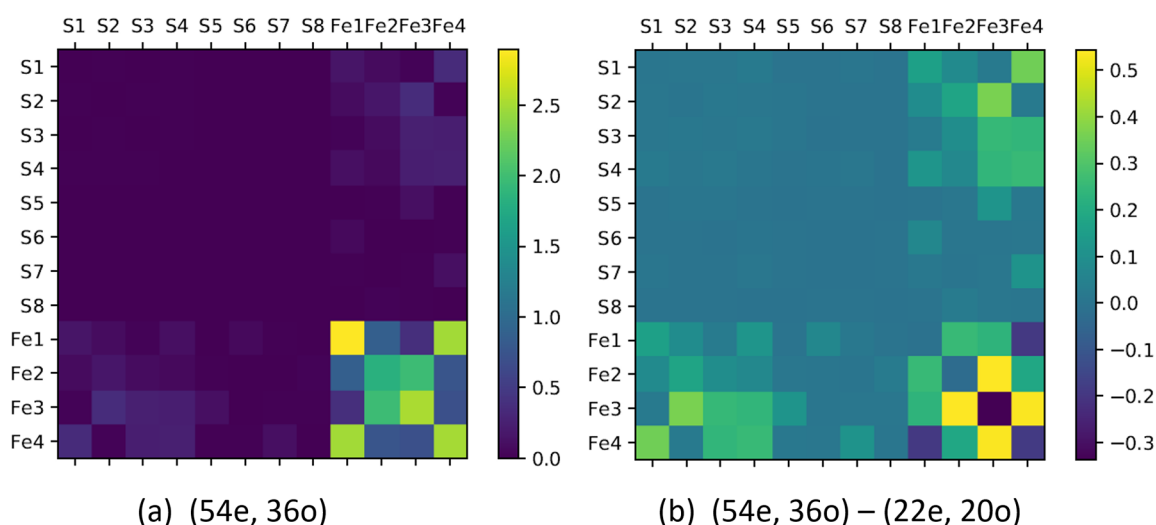


**Figure 5.** Mutual information for the 2A cluster, singlet state, between different orbital groups. Fe<sub>*i*</sub> corresponds to the valence 3*d*-orbitals of the *i*-th Fe atom, while S<sub>*i*</sub> refers to the valence 3*p*-orbitals of the *i*-th S atom. The left panel shows the mutual information computed from the ROHF localized orbitals using the (54e, 36o) active space, while the right panel shows the difference between the results using the (54e, 36o) and (22e, 20o) active spaces.

However, not all optimized orbitals in the active space follow the previous scheme as nicely as shown in Figure 2. In particular, throughout all geometries and spin states, several of the S-3*p* and Fe-3*d* orbitals in the (54e, 36o) active space get substituted by Fe-3*p* orbitals during the CASSCF calculations. These orbitals are nonetheless otherwise unmixed with the rest of the active space constituents and given their nonvalence character seem unlikely to play a relevant role in the reactive properties of these clusters. To discern whether the inclusion of Fe-3*p* orbitals is an artifact of the optimization or actually important from a physical point of view, we consider CASSCF calculations on the 2A geometry with various active space sizes in the next section.

**4.4. The Effect of the Active Space.** As mentioned in section 2, whether CASSCF captures the correct physical behavior can be active space dependent, especially in strongly correlated systems, such as iron-based clusters.<sup>41</sup> Therefore, we consider in this subsection the effect of the active space choice in the example of geometry 2A, the variationally most stable geometry we consider, both at the mean-field and correlated treatments. Given the previous discussion on the antiferromagnetic coupling between high-spin Fe-dimers, it is likely that the 2A geometry is the most stable because it has the shortest relative Fe–Fe dimer bond length within the high spin dimers, as discussed in the beginning of this section. In this cluster, the high-spin dimers present a bond length ~11% smaller than the others Fe–Fe bonds, while for 2B-R the high spin dimers show only ~3% shorter bonds.

Here, we consider the four different active spaces described in detail in section 2: (22e, 20o), which only includes Fe-3*d* orbitals, (46e, 32o), which additionally includes the 12 S-3*p* orbitals from the bridging S atoms, but excluding the ligand S orbitals, (54e, 36o), recovering the four ligand S-3*p* orbitals pointing toward the Fe atoms, and finally (86e, 52o), which also includes the 12 Fe-3*p* and four Fe-3*s* orbitals. This largest active space is meant to address the “orbital intrusion” observed above for the CASSCF calculations in the (54e, 36o) active space: the unexpected exchange of some of the active orbitals by Fe-3*p* ones. One way to deal with this intrusion would be constraining the CASSCF optimization to

not include the “unwanted” orbitals, either by freezing them in the optimization or by reordering the orbitals between subsequent CASSCF cycles. Instead, we chose a less biased approach, and expand the (54e, 36o) active space by including the 12 Fe-3*p* and four Fe-3*s* orbitals, the *s* added to account for *sp* hybridization. This way, we can unambiguously determine whether the Fe-3*p/s* orbitals are actually important to describe the electronic correlation.

For all the active spaces described above, we perform CASSCF calculations with the SP-ASCI solver following the exact same procedure as with the (54e, 36o) active space in the previous section, starting from Pepek-Mezey localized HS-ROHF orbitals. We report the CASSCF and ASCI+PT2 extrapolated energies for the different active spaces, and three lowest lying spin states for cluster geometry 2A in Table 5.

Examining the CASSCF energies in Table 5, it becomes clear that the minimal active space (22e, 20o) misses, as expected, a significant amount of the correlation energy, having a gap with respect to the next active space (46e, 32o) of ~50 mHa (~1.4 eV). Furthermore, compared with the high-spin ROHF energy in Table 1, the (22e, 20o) active space is only ~5 mHa (~140 meV) lower in energy (we observe a similar behavior in the Fe<sub>3</sub> results with the (15e, 15o) active space in the SI). Upon further increase of the active space, we observe additional stabilization energies: the ligand S-3*p* orbitals recover ~10 mHa (~280 meV), and the Fe-3*p* and Fe-*s* orbitals surprisingly account for an additional ~20 mHa (~560 meV). The fact that the Fe-3*s,3p* orbitals account for a comparable amount of correlation energy than the ligand S-3*p* indicates that an accurate treatment of the electronic structure requires both sets, suggesting that larger active spaces than are usually considered are likely key to accurately predicting the electrochemical properties of iron–sulfur systems. Similar conclusions have been drawn from single-point selective CI and DMRG calculations on the FeMoco cofactor.<sup>65</sup> This notion could explain the observation, noted above, that optimized orbitals in both the (46e, 32o) and (54e, 36o) active spaces end up including some Fe-3*p* orbitals after the ASCI-SCF calculation.

**Table 5. CASSCF and Extrapolated Energies ( $E - 8380.0$  Ha) Using SP-ASCI Different Active Spaces for the 2A Geometry of the  $[\text{Fe}_4\text{S}_4(\text{SMe})_4]^{-2}$  Cluster, Starting from the High Spin ( $2S + 1 = 19$ ) ROHF Orbitals, Localized with the Pipek–Mezey Scheme<sup>a</sup>**

act. space	2S + 1	CASSCF SP-ASCI-SCF	ASCI + PT2 extrapol. SP-ASCI
(22e, 20o)	5	-9.088122	-9.088360 ± 0.000037
	3	-9.088318	-9.088575 ± 0.000002
	1	-9.088439	-9.088638 ± 0.000010
(46e, 32o)	5	-9.142546	-9.1483 ± 0.0005
	3	-9.142428	-9.1472 ± 0.0007
	1	-9.142759	-9.1470 ± 0.0004
(54e, 36o)	5	-9.150451	-9.1553 ± 0.0010
	3	-9.150856	-9.1554 ± 0.0008
	1	-9.150950	-9.1554 ± 0.0007
(86e, 52o)	5	-9.171896	-9.1789 ± 0.0005
	3	-9.171579	-9.1789 ± 0.0007
	1	-9.171783	-9.1788 ± 0.0007

<sup>a</sup>All calculations are performed with the mixed aug-cc-pVDZ (Fe,S) cc-pVDZ (C,H) basis set. The CASSCF energies correspond to SP-ASCI calculations with  $5 \times 10^6$  determinants. These correspond to the final step of a series of SP-ASCI-SCF calculations starting at  $1 \times 10^5$  determinants, and progressively increasing the number of determinants to improve the orbitals sequentially. The ASCI+PT2 extrapolated results are estimating the FCI limit, using a linear extrapolation from calculations with  $5 \times 10^5$ ,  $1 \times 10^6$ ,  $2 \times 10^6$ , and  $5 \times 10^6$  determinants, starting from the orbitals obtained from the SP-ASCI-SCF with  $5 \times 10^6$  determinants. The (22e, 20o) extrapolation converged by the  $2 \times 10^6$  determinant calculation, the (86e, 52o) one was extended to  $7 \times 10^6$  determinants. The error bars correspond to the standard deviation of the linear fit and are, thus, just a measure of the extrapolation error alone. For the quintet (86e, 52o) extrapolation, the  $10^6$  determinant calculation was disregarded as an outlier.

In Figure 6, we summarize the correlation energy per electron obtained by including each new set of orbitals into the correlated CASSCF SP-ASCI calculation for the 2A cluster geometry, as well as the correlation energy per electron in the Fe-3d orbitals for one of the  $[\text{Fe}_3\text{S}_4(\text{SMe})_3]^{-2}$  clusters included in the SI. As mentioned before, the correlation energy resulting from the 3d electrons is very small, about 0.2 mHa/e<sup>-</sup> (5.4

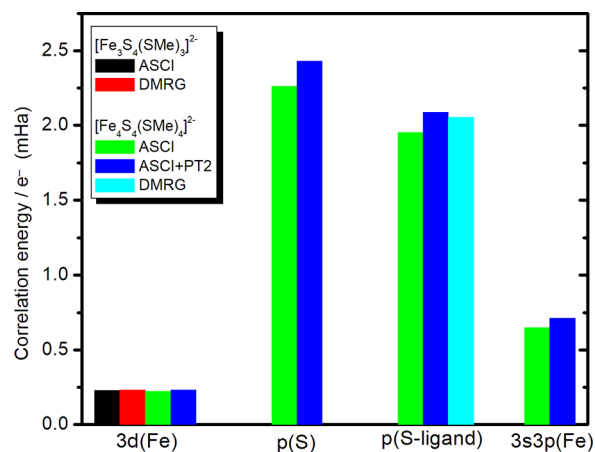


**Figure 6.** Correlation energy of Fe-3d, S-3p, and Fe-3s3p electrons in the 2A geometry of the  $[\text{Fe}_4\text{S}_4(\text{SMe})_4]^{-2}$  cluster, and of Fe-3d orbitals for the 1A geometry of the  $[\text{Fe}_3\text{S}_4(\text{SMe})_3]^{-2}$  cluster.

meV/e<sup>-</sup>) at ASCI and DMRG, see Figure 6, for both clusters. This is the reason the states are energetically degenerate for different spin multiplicities. The correlation energy results mainly from the 3p electrons of S, and it is significantly larger than the 3d electrons of Fe, that is, 2.5 mHa/e<sup>-</sup> (68 meV/e<sup>-</sup>) for the 3p electron of S bridge and 2.0 mHa/e<sup>-</sup> (54 meV/e<sup>-</sup>) for 3p electron of S ligand. It is interesting that the correlation of the 3s and 3p electrons of Fe is 0.7 mHa/e<sup>-</sup> (19 meV/e<sup>-</sup>). The correlation that stems from S-3p orbitals can be attributed to two complementary reasons: (i) the S-3p orbitals are essentially doubly occupied, but there is an interaction with the low-lying empty 4s orbitals of the Fe<sup>2+</sup>(<sup>5</sup>D, 3d<sup>6</sup>) and Fe<sup>3+</sup>(<sup>6</sup>S, 3d<sup>5</sup>) (see SI); and (ii) the double-exchange interaction of half occupied Fe-3d and S-3p orbitals, where both the Fe-3d and S-3p orbitals need to be included in the active space to account for the correlation energy. Finally, the correlation because of the Fe-(3p/3s) orbitals results from the fact that these orbitals have the right symmetry to couple to both the Fe-3d orbitals and with the empty Fe-4s ones.

The previous energetic considerations thus seem to suggest that it is necessary to include all S-3p and even further the Fe-3p/3s orbitals into the active space for an accurate description of ground state of these iron–sulfur clusters. Still, when examining the charge densities of these CASSCF optimized orbitals for the different active spaces (i.e., the diagonal elements of the 1-RDMs), represented in the upper panel of Figure 4 for the 2A geometry in the singlet state, we see that even when treated explicitly, the Fe-3s,3p orbitals, and indeed the S-3p/Fe-3d molecular orbitals, are effectively inactive, that is, consistently doubly occupied in the wave function. Rotating the corresponding 1-RDM into the localized ROHF basis, we can compute the charge densities of the atomic Fe-3s/3p/3d and S-3p orbitals, shown in the lower panel of Figure 4. While this unveils some degree of charge transfer between the Fe-3d and S-3p orbitals further supporting a double-exchange mechanism, the Fe-3s/3p orbitals remain essentially inactive, with no appreciable charge fluctuations away from them. For the Fe-3s/3p orbitals this suggests that the origin of the energy lowering upon their inclusion in the active space may arise because of an improvement in the orbital optimization process.

Like in the previous section, we examine the spin–spin correlation functions within the Fe-3d orbitals for the 2A geometry singlet, triplet and quintet states as a function of the active space size in Figure 7. In the basis of CASSCF optimized orbitals (left panels), we see that the picture discussed in Figure 3 is independent of the size of the active space. Even the small (22e, 20o) active space, which only includes Fe-3d orbitals explicitly, can capture the organization of the four Fe atoms into two high-spin Fe-dimers which couple antiferromagnetically to account for, essentially, the full spin state of the cluster. When rotating the correlation functions back into the localized ROHF basis, we once again observe some degree of spin fluctuation away from the Fe-3d orbitals: the Fe-dimers have lower effective spin multiplicity (upper right panel in Figure 7), and the Fe-3d orbitals do not account for the spin state of the full cluster (lower right panel in Figure 7). The results are essentially independent of the active space, except for the fact that in the (46e, 32o) active space, the two high-spin Fe-dimers show different effective multiplicities.

From the present discussion, we see that the smallest active space (22e, 20o) describes static properties, such as charge densities and spin–spin correlations, equally well than more complex active spaces including S-3p and Fe-3s/3p orbitals.

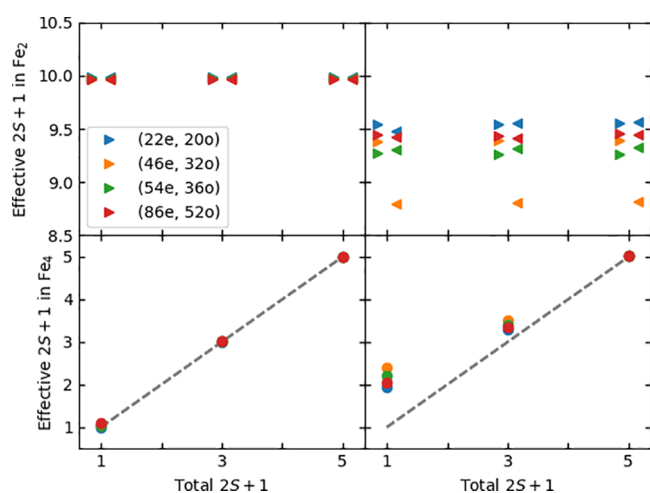


**Figure 7.** Effective spin multiplicity  $2S + 1$  for different subsets of Fe-3d orbitals from the CASSCF optimized SP-ASCI wave functions of the 2A geometry in the (aug)-cc-pVDZ basis set and different active spaces. Upper panels: Multiplicities considering the Fe-3d orbitals of the two ferromagnetically coupled Fe-dimers within the Fe4 cluster. The left panel is computed in the CASSCF basis, the right panel is rotated to the localized ROHF basis. Lower panels: Multiplicities considering the Fe-3d orbitals of all four Fe atoms, in the CASSCF basis (left) and rotated to the localized ROHF basis (right). See text for details.

The orbital optimization in the CASSCF procedure seems to compensate for the lack in active orbitals. Still, considering the change in correlation energy by active space, see Figure 6, the Fe-3d orbitals alone cannot account for anything but a minute part of the correlation, and it is necessary to include all Fe-3d, S-3p, and apparently Fe-3s/3p, in the active space to capture the correlation energy. These observations seem to contradict each other. A possible reconciliation would be to check whether the correlation energy due to the S-3p and Fe-3s/3p orbitals can be recovered perturbatively from the (22e, 20o) ground state wave function. This would explain both the consistent static properties across active spaces, as well as the sizable correlation energy due to the S-3p and Fe-3s/3p orbitals. We checked this by computing the ASCI+PT2 energies for the 2A singlet state starting from the (22e, 20o) active space wave function with 2 million determinants, but including the S-3p and Fe-3s/3p orbitals for the perturbative correction. However, this could only account for  $\sim 5$  mHa, which is only  $\sim 10\%$  of the total correlation energies in Figure 6. The S-3p and Fe-3s/3p orbitals seem to be needed explicitly in the active space in order to capture the correlation energy accurately. Our results suggest that static properties, within the orbitals considered explicitly here, can be captured in the CASSCF orbital rotation independently of whether these orbitals are inside the active space, while dynamical information such as correlation energies require an explicit description within the active space.

Finally, it is interesting to note the progression of the energy gap between the smallest and largest spin states ( $2S + 1 = 1$  and  $2S + 1 = 19$ , respectively) as a function of the active space, which we summarize in Table 6. The energies of the high spin state are obtained using the CASSCF optimized orbitals for the singlet state, with enough determinants to converge the energy to sub mHa accuracy ( $5 \times 10^5$  for all active spaces instead of the largest one, which needed  $10^6$ ). Optimizing the orbitals for the high spin state explicitly does not change the energies

**Table 6.** SP-ASCI Energies ( $E - 8380.0$  Ha), Plus PT2 Correction in Parentheses, for the High Spin State  $2S + 1 = 19$  in the 2A Geometry for Different Active Spaces<sup>a</sup>

act. space	$2S + 1 = 19$ energy [Ha] SP-ASCI (PT2)	variational gap [meV]	extrapolated gap [meV]
(22e, 20o)	-9.082663 (0)	-157.8	-163.3
(46e, 32o)	-9.140243 (-0.000009)	-68.0	-182.3
(54e, 36o)	-9.149945 (-0.000020)	-27.2	-149.7
(86e, 52o)	-9.173713 (-0.000054)	51.7	-136.1

<sup>a</sup>We use the CASSCF optimized orbitals from the singlet state. The last two columns summarize the spin gaps in meV between the high spin and singlet states, computed as  $E_0^{2S+1=1} - E_0^{2S+1=19}$ , where the corresponding singlet energies were taken from Table 5. We report variational spin gaps, as well as extrapolated spin gaps including the PT2 correction.

significantly (differences being within  $\sim 1$ – $2$  mHa). We observe a monotonic decrease in the spin gap with increasing active space when using variational SP-ASCI energies, up to a change in sign in the (86e, 52o) resulting in the high spin state being lower in energy than all low-spin states. Upon recovering dynamical correlation with second order perturbation theory, the singlet state becomes stabilized with respect to the high spin state, regardless of the active space size. Further, we observe a relatively active-space independent energy gap of  $\sim 150$  meV ( $\sim 5.5$  mHa), with a nonmonotonic convergence which falls however within our numerical uncertainty. Dynamical correlation beyond the active space would need to be recovered to make accurate statements beyond our  $\sim 1$  mHa ( $\sim 27$  meV) accuracy.

## 5. CONCLUSIONS

In this work, we have for the first time used CASSCF with large active spaces to study model systems for Fe-based catalytic centers, namely, the  $[\text{Fe}_4\text{S}_4(\text{SMe})_4]^{-2}$  cubanes, paying special attention to the role of geometry and spin state in the system's properties. We have employed highly accurate and complementary correlated solvers for the CASSCF problem, namely, ASCI and DMRG. The good agreement between these two techniques gives us confidence in our results, and further shows that it is now possible to treat these highly complex systems with sophisticated many-body approaches such as CASSCF. Moreover, we have introduced the SP-ASCI approach, which proposes Hilbert space truncations preserving spin conservation by modifying the ASCI search in terms of CSF families. While SP-ASCI shows severe convergence issues in the mean-field single-particle basis studied, that is, localized ROHF, using it as solver for CASSCF remedies this limitation and provides accurate results in good agreement with DMRG.

Our results show that orbital optimization improves the energies of different spin states significantly, reduces the spin energy gaps with respect to ROHF, and also brings to the forefront the underlying physical mechanism that dominates the system. Indeed, the optimized single-particle orbital basis is reminiscent of the double-exchange mechanism widely accepted to be responsible for the magnetic structure of these Fe–S clusters. Since single-particle orbitals are not physically well-defined, we complement this interpretation with one-electron, two-electron, and two-orbital correlation

functions, namely, charge densities, spin–spin correlations and mutual information. All these diagnostics support the double-exchange interpretation, and are consistent across different active spaces, geometries, and spin states.

All geometries show essentially degenerate spin states with gaps between successive spin states being of the order of 1 mHa or lower. This is explained by examining the correlation energy as a function of active space size, which shows that the Fe-3d electrons alone do not contribute to it significantly. Since the spin state is essentially determined by the Fe-3d electrons, their near-degeneracy is not unexpected. The correlation energy comes in comparable amounts from bridge S-3p, ligand S-3p, as well as Fe-3s/3p orbitals. The nontrivial correlation that stems from these orbitals can be attributed to two complementary reasons: (i) the S-3p orbitals are essentially doubly occupied, but there is an interaction with the low-lying energy empty 4s orbitals of Fe(II) and Fe(III) and (ii) the double-exchange interaction of half occupied Fe-3d and S-3p orbitals, where both the Fe-3d and S-3p orbitals are needed to be treated in the active space in order to account for the correlation energy. Finally, the correlation due to the Fe-(3p/3s) orbitals results from the fact that these orbitals have the right symmetry to couple to the Fe-3d orbitals and with the empty Fe-4s ones. To capture all this contributions accurately, it is necessary to include all these orbitals into the active space, as simple perturbative corrections on top of smaller active spaces do not seem capable of accounting for them.

While the small gaps between consecutive spin states makes a definite statement about detailed spin hierarchies difficult, we observe a significant geometry dependence of the largest spin gap, defined as the energy difference between the singlet and largest spin state. By arranging the Fe-atoms slightly asymmetrically, forming two dimers of ~11% shorter bond length, this maximal gap is reduced by approximately a factor of 3. It is this fine-tuning of spin-dependent energetics by subtle geometry changes that makes Fe–S-based enzymes remarkable catalysts in biological systems. The reduction of spin energy gaps upon CASSCF orbital optimization, as well as the lifting of apparent degeneracies between slightly different geometries when going from the BS-DFT level to CASSCF, indicate that this type of sophisticated electronic structure treatment will likely prove crucial for an accurate description of the reactivity in these correlated systems. The next step toward a fully correlated treatment of these complexes would require describing the dynamical correlation beyond the active space. While this is likely to have a strong impact on the spin ordering of states, our observed geometry dependence of singlet-to-high-spin gaps should remain representative of the true physics of these systems. We note that CI-based solvers for CASSCF similar to the one employed in this work are being developed and tested concurrently.<sup>31,101</sup> Finally, it has been reported recently that DFT-based methods are unreliable to predict the relative energy ordering of possible isomers of cofactors, such as the FeMoCo in nitrogenase,<sup>102</sup> while BS-DFT may also have problems predicting the correct spin state even of the electronic ground state for complex multispin systems, that is, for systems having more than one transition metal cations.<sup>27,103,104</sup> However, given their low computational cost, these methods are likely to remain widely used to treat these complex systems. In this regard, a useful and important scope of our work is to provide an accurate description of the

challenging electronic structure of iron–sulfur cubanes that can be used as benchmark for DFT-based calculations.

## ■ ASSOCIATED CONTENT

### SI Supporting Information

The Supporting Information is available free of charge at <https://pubs.acs.org/doi/10.1021/acs.jctc.1c00830>.

.xyz files for the clusters (ZIP)

Detailed presentation of the ASCI-based algorithms, a discussion of the ROHF starting points, results for five geometries of Fe<sub>3</sub> clusters, tabulated values of Fe–Fe and Fe–S bond lengths, as well as Fe–S–Fe angles for the four [Fe<sub>4</sub>S<sub>4</sub>(SCH<sub>3</sub>)<sub>4</sub>]<sup>−2</sup> geometries, an analysis of the Fe-4s orbital component in the different CASSCF optimized molecular orbitals, number of determinants and CSF's of the right spin for the largest ASCI calculations of the Fe<sub>4</sub> clusters, results for the 2R geometry with the def2-SVP basis set, and a brief comment on basis set choice (PDF)

## ■ AUTHOR INFORMATION

### Corresponding Authors

**Carlos Mejuto-Zaera** – University of California, Berkeley, California 94720, United States; Computational Research Division, Lawrence Berkeley National Laboratory, Berkeley, California 94720, United States; [orcid.org/0000-0001-5921-0959](https://orcid.org/0000-0001-5921-0959); Email: [carlos\\_mejutozaera@berkeley.edu](mailto:carlos_mejutozaera@berkeley.edu)

**Norm M. Tubman** – Quantum Artificial Intelligence Lab. (QuAIL), Exploration Technology Directorate, NASA Ames Research Center, Moffett Field, California 94035, United States; [orcid.org/0000-0002-9577-8485](https://orcid.org/0000-0002-9577-8485); Email: [norman.m.tubman@nasa.gov](mailto:norman.m.tubman@nasa.gov)

**Libor Veis** – J. Heyrovský Institute of Physical Chemistry, Academy of Sciences of the Czech Republic, v.v.i., 18223 Prague 8, Czech Republic; [orcid.org/0000-0002-4229-6335](https://orcid.org/0000-0002-4229-6335); Email: [libor.veis@jh-inst.cas.cz](mailto:libor.veis@jh-inst.cas.cz)

**Sotiris S. Xantheas** – Advanced Computing, Mathematics and Data Division, Pacific Northwest National Laboratory, Richland, Washington 99352, United States; Department of Chemistry, University of Washington, Seattle, Washington 98185, United States; [orcid.org/0000-0002-6303-1037](https://orcid.org/0000-0002-6303-1037); Email: [sotiris.xantheas@pnnl.gov](mailto:sotiris.xantheas@pnnl.gov)

**Wibe A. de Jong** – Computational Research Division, Lawrence Berkeley National Laboratory, Berkeley, California 94720, United States; [orcid.org/0000-0002-7114-8315](https://orcid.org/0000-0002-7114-8315); Email: [WAdeJong@lbl.gov](mailto:WAdeJong@lbl.gov)

### Authors

**Demeter Tzeli** – Laboratory of Physical Chemistry, Department of Chemistry, National and Kapodistrian University of Athens, Panepistimiopolis Zografou, Athens 15784, Greece; Theoretical and Physical Chemistry Institute, National Hellenic Research Foundation, Athens 11635, Greece

**David Williams-Young** – Computational Research Division, Lawrence Berkeley National Laboratory, Berkeley, California 94720, United States; [orcid.org/0000-0003-2735-3706](https://orcid.org/0000-0003-2735-3706)

**Mikuláš Matoušek** – J. Heyrovský Institute of Physical Chemistry, Academy of Sciences of the Czech Republic, v.v.i., 18223 Prague 8, Czech Republic

**Jiri Brabec** – J. Heyrovský Institute of Physical Chemistry, Academy of Sciences of the Czech Republic, v.v.i., 18223

Prague 8, Czech Republic; [orcid.org/0000-0002-7764-9890](https://orcid.org/0000-0002-7764-9890)

Complete contact information is available at:  
<https://pubs.acs.org/10.1021/acs.jctc.1c00830>

### Author Contributions

D.T., W.A.J., and S.S.X. proposed the original research; N.T., L.V., S.S.X., and W.A.J. supervised different aspects of the project. D.T. performed the BS-DFT geometry optimizations and initial CASSCF calculations; C.M.Z. performed the ASCI-SCF calculations and developed the spin-pure (SP) variant of ASCI; M.M., J.B., and L.V. performed the DMRG calculations. D.W.Y. and N.T. contributed to the ASCI code. C.M.Z., D.T., and L.V. wrote the manuscript. All authors contributed to the analysis and discussion of the results and reviewed and modified the manuscript.

### Notes

The authors declare no competing financial interest.

### ACKNOWLEDGMENTS

We wish to thank Dr. Simone Raugei of the Pacific Northwest National Laboratory for useful suggestions and discussions. D.T., J.B., L.V., C.M.Z., S.S.X., and W.A.J. acknowledge support from the Center for Scalable Predictive methods for Excitations and Correlated phenomena (SPEC), which is funded by the U.S. Department of Energy, Office of Science, Basic Energy Sciences, Chemical Sciences, Geosciences and Biosciences Division, as part of the Computational Chemical Sciences Program at Pacific Northwest National Laboratory. Battelle operates the Pacific Northwest National Laboratory for the U.S. Department of Energy. This manuscript has been authored by an author at Lawrence Berkeley National Laboratory under Contract No. DE-AC02-05CH11231 with the U.S. Department of Energy. N.M.T. is grateful for support from NASA Ames Research Center and support from the AFRL Information Directorate under Grant No. F4HBKC4162G00. L.V. acknowledges support from Czech Science Foundation (Grant 18-18940Y). The calculations were performed as part of the XSEDE computational Project No. TG-MCA93S030. This research also used resources of the National Energy Research Scientific Computing Center, which is supported by the Office of Science of the U.S. Department of Energy under Contract No. DE-AC02-05CH11231 and resources of the Czech supercomputing center supported by the Czech Ministry of Education, Youth and Sports from the Large Infrastructures for Research, Experimental Development and Innovations project "IT4Innovations LM2015070."

### REFERENCES

- (1) Spiro, T. G. *Iron–Sulfur Proteins*; Wiley-Interscience: New York, 1982.
- (2) Holm, R. H.; Kennepohl, P.; Solomon, E. I. Structural and Functional Aspects of Metal Sites in Biology. *Chem. Rev.* **1996**, *96*, 2239–2314.
- (3) Kessler, D.; Papenbrock, J. Iron-sulfur cluster biosynthesis in photosynthetic organisms. *Photosynthesis Research* **2005**, *86*, 391–407.
- (4) Jang, S.; Seefeldt, L. C.; Peters, J. W. Insights into Nucleotide Signal Transduction in Nitrogenase: Structure of an Iron Protein with MgADP Bound. *Biochemistry* **2000**, *39*, 14745–14752.
- (5) Brzóska, K.; Meczynska, S.; Kruszewski, M. Iron-sulfur cluster proteins: electron transfer and beyond. *Acta Biochim Pol* **2006**, *53*, 685–91.

- (6) Einsle, O.; Tezcan, F. A.; Andrade, S. L. A.; Schmid, B.; Yoshida, M.; Howard, J. B.; Rees, D. C. Nitrogenase MoFe-Protein at 1.16 Å Resolution: A Central Ligand in the FeMo-Cofactor. *Science* **2002**, *297*, 1696–1700.
- (7) Doukov, T. I.; Iverson, T. M.; Seravalli, J.; Ragsdale, S. W.; Drennan, C. L. A Ni-Fe-Cu Center in a Bifunctional Carbon Monoxide Dehydrogenase/Acetyl-CoA Synthase. *Science* **2002**, *298*, 567–572.
- (8) Berkovitch, F.; Nicolet, Y.; Wan, J. T.; Jarrett, J. T.; Drennan, C. L. Crystal Structure of Biotin Synthase, an S-Adenosylmethionine-Dependent Radical Enzyme. *Science* **2004**, *303*, 76–79.
- (9) Munck, E.; Bominaar, E. L. Chemistry – bringing stability to highly reduced iron-sulfur clusters. *Science* **2008**, *321*, 1452–1453.
- (10) Lukianova, O. A.; David, S. S. A role for iron-sulfur clusters in DNA repair. *Curr. Opin. Chem. Biol.* **2005**, *9*, 145–151.
- (11) Kiley, P. J.; Beinert, H. The role of Fe-S proteins in sensing and regulation in bacteria. *Curr. Opin. Microbiol.* **2003**, *6*, 181–185.
- (12) Beinert, H.; Holm, R. H.; Münck, E. Iron-Sulfur Clusters: Nature's Modular, Multipurpose Structures. *Science* **1997**, *277*, 653–659.
- (13) Runyen-Janecky, L.; Daugherty, A.; Lloyd, B.; Wellington, C.; Eskandarian, H.; Sagransky, M. Role and Regulation of Iron-Sulfur Cluster Biosynthesis Genes in *Shigella flexneri* Virulence. *Infect. Immun.* **2008**, *76*, 1083–1092.
- (14) Wofford, J. D.; Lindahl, P. A. Mitochondrial Iron-Sulfur Cluster Activity and Cytosolic Iron Regulate Iron Traffic in *Saccharomyces cerevisiae*. *J. Biol. Chem.* **2015**, *290*, 26968–77.
- (15) Rees, D. C.; Howard, J. B. The interface between the biological and inorganic worlds: iron-sulfur metalloclusters. *Science* **2003**, *300*, 929–931.
- (16) Nurmaganbetova, M. S.; Baikenov, M. I.; Meiramov, M. G.; Mukhtar, A. A.; Ordabaeva, A. T.; Khрупov, V. A. Catalytic hydrogenation of anthracene on modified iron sulfide catalysts. *Pet. Chem.* **2001**, *41*, 26–29.
- (17) Dance, I. Electronic Dimensions of FeMo-co, the Active Site of Nitrogenase, and Its Catalytic Intermediates. *Inorg. Chem.* **2011**, *50*, 178–192.
- (18) Ghosh, A. C.; Duboc, C.; Gennari, M. Synergy between metals for small molecule activation: Enzymes and bio-inspired complexes. *Coord. Chem. Rev.* **2021**, *428*, 213606.
- (19) Noodleman, L.; Case, D. A.; Aizman, A. Broken Symmetry Analysis of Spin Coupling in Iron-Sulfur Clusters. *J. Am. Chem. Soc.* **1988**, *110*, 1001–1005.
- (20) Sigfridsson, E.; Olsson, M. H. M.; Ryde, U. Inner-Sphere Reorganization Energy of Iron-Sulfur Clusters Studied with Theoretical Methods. *Inorg. Chem.* **2001**, *40*, 2509–2519.
- (21) Niu, S.; Ichiye, T. Cleavage of [4FeS4]-Type Clusters: Breaking the Symmetry. *J. Phys. Chem. A* **2009**, *113*, 5710–5717.
- (22) Dance, I. Protonation of bridging sulfur in cubanoid Fe4S4 clusters causes large geometric changes: the theory of geometric and electronic structure. *Dalton Trans.* **2015**, *44*, 4707–4717.
- (23) Bergeler, M.; Stiebritz, M. T.; Reiher, M. Structure–Property Relationships of Fe4S4 Clusters. *ChemPlusChem.* **2013**, *78*, 1082–1098.
- (24) Carvalho, A. T. P.; Swart, M. Electronic Structure Investigation and Parametrization of Biologically Relevant Iron-Sulfur Clusters. *J. Chem. Inf. Model.* **2014**, *54*, 613–620.
- (25) Neese, F. Prediction of molecular properties and molecular spectroscopy with density functional theory: from fundamental theory to exchange-coupling. *Coord. Chem. Rev.* **2009**, *253*, 526–563.
- (26) Sharma, S.; Sivalingam, K.; Neese, F.; Chan, G. K.-L. Low-energy spectrum of iron-sulfur clusters directly from many-particle quantum mechanics. *Nature Chem.* **2014**, *6*, 927–933.
- (27) Rudra, I.; Wu, Q.; Van Voorhis, T. Predicting Exchange Coupling Constants in Frustrated Molecular Magnets Using Density Functional Theory. *In. Chem.* **2007**, *46*, 10539.
- (28) Schipke, C. G.; Goodin, D. B.; McRee, D. E.; Stout, C. D. Oxidized and Reduced *Azotobacter vinelandii* Ferredoxin I at 1.4 Å Resolution: Conformational Change of Surface Residues without

- Significant Change in the  $[3\text{Fe-4S}]^{+}/0$  Cluster. *Biochemistry* **1999**, *38*, 8228–8293.
- (29) Kissinger, C. R.; Sieker, L. C.; Adman, E. T.; Jensen, J. L. Refined crystal structure of ferredoxin II from *Desulfovibrio gigas* at 1.7 Å. *J. Mol. Biol.* **1991**, *219*, 693–715.
- (30) Small, D. W.; Head-Gordon, M. Independent amplitude approximations in coupled cluster valence bond theory: Incorporation of 3-electron-pair correlation and application to spin frustration in the low-lying excited states of a ferredoxin-type tetrametallic iron-sulfur cluster. *J. Chem. Phys.* **2018**, *149*, 144103.
- (31) Dobrutz, W.; Weser, O.; Bogdanov, N.; Alavi, A.; Manni, G. L. Spin-pure Stochastic-CASSCF via GUGA-FCIQMC applied to Iron Sulfur Clusters. *arXiv*, 2021, 2106.07775. <https://arxiv.org/abs/2106.07775>.
- (32) Presti, D.; Stoneburner, S. J.; Truhlar, D. G.; Gagliardi, L. Full Correlation in a Multiconfigurational Study of Bimetallic Clusters: Restricted Active Space Pair-Density Functional Theory Study of  $[2\text{Fe-2S}]$  Systems. *J. Phys. Chem. C* **2019**, *123*, 11899–11907.
- (33) Tubman, N. M.; Lee, J.; Takeshita, T. Y.; Head-Gordon, M.; Whaley, K. B. A deterministic alternative to the full configuration interaction quantum Monte Carlo method. *J. Chem. Phys.* **2016**, *145*, 044112.
- (34) Tubman, N. M.; Levine, D. S.; Hait, D.; Head-Gordon, M.; Whaley, K. B. An efficient deterministic perturbation theory for selected configuration interaction methods. *arXiv*, 2018, 1808.02049v1. <https://arxiv.org/abs/1808.02049v1>.
- (35) Tubman, N. M.; Freeman, C. D.; Levine, D. S.; Hait, D.; Head-Gordon, M.; Whaley, K. B. Modern approaches to exact diagonalization and selected configuration interaction with the adaptive sampling CI method. *J. Chem. Theory Comput.* **2020**, *16*, 2139–2159.
- (36) White, S. R. Density matrix formulation for quantum renormalization groups. *Physical review letters* **1992**, *69*, 2863.
- (37) Schollwöck, U. The density-matrix renormalization group in the age of matrix product states. *Annals of physics* **2011**, *326*, 96–192.
- (38) Chan, G. K.-L.; Sharma, S. The density matrix renormalization group in quantum chemistry. *Annu. Rev. Phys. Chem.* **2011**, *62*, 465–481.
- (39) Helgaker, T.; Jorgensen, P.; Olsen, J. *Molecular Electronic Structure Theory*; Wiley, New York, 2000.
- (40) Wouters, S.; Bogaerts, T.; Van Der Voort, P.; Van Speybroeck, V.; Van Neck, D. Communication: DMRG-SCF study of the singlet, triplet, and quintet states of oxo-Mn (Salen). *J. Chem. Phys.* **2014**, *140*, No. 241103, DOI: 10.1063/1.4885815.
- (41) Levine, D. S.; Hait, D.; Tubman, N. M.; Lehtola, S.; Whaley, K. B.; Head-Gordon, M. CASSCF with Extremely Large Active Spaces using the Adaptive Sampling Configuration Interaction Method. *J. Chem. Theory Comput.* **2020**, *16*, 2340–2354.
- (42) Brabec, J.; Brandeys, J.; Kowalski, K.; Xantheas, S.; Legeza, Ö.; Veis, L. Massively parallel quantum chemical density matrix renormalization group method. *J. Comput. Chem.* **2021**, *42*, 534–544.
- (43) Huron, B.; Malrieu, J.; Rancurel, P. Iterative perturbation calculations of ground and excited state energies from multiconfigurational zeroth-order wavefunctions. *J. Chem. Phys.* **1973**, *58*, 5745–5759.
- (44) Evangelisti, S.; Daudey, J.-P.; Malrieu, J.-P. Convergence of an improved CIPSI algorithm. *Chem. Phys.* **1983**, *75*, 91–102.
- (45) Illas, F.; Rubio, J.; Ricart, J.; Bagus, P. Selected versus complete configuration interaction expansions. *J. Chem. Phys.* **1991**, *95*, 1877–1883.
- (46) Tubman, N. M.; Mejuto-Zaera, C.; Epstein, J. M.; Hait, D.; Levine, D. S.; Huggins, W.; Jiang, Z.; McClean, J. R.; Babbush, R.; Head-Gordon, M. et al. Postponing the orthogonality catastrophe: efficient state preparation for electronic structure simulations on quantum devices. *arXiv*, 2018, 1809.05523. <https://arxiv.org/abs/1809.05523>.
- (47) Mejuto-Zaera, C.; Tubman, N. M.; Whaley, K. B. Dynamical mean field theory simulations with the adaptive sampling configuration interaction method. *Phys. Rev. B* **2019**, *100*, 125165.
- (48) Hait, D.; Tubman, N. M.; Levine, D. S.; Whaley, K. B.; Head-Gordon, M. What Levels of Coupled Cluster Theory Are Appropriate for Transition Metal Systems? A Study Using Near-Exact Quantum Chemical Values for 3d Transition Metal Binary Compounds. *J. Chem. Theory Comput.* **2019**, *15*, 5370–5385.
- (49) Mejuto-Zaera, C.; Weng, G.; Romanova, M.; Cotton, S. J.; Whaley, K. B.; Tubman, N. M.; Vlček, V. Communication: Are multi-quasiparticle interactions important in molecular ionization?? *J. Chem. Phys.* **2021**, *154*, 121101.
- (50) Eriksen, J. J.; Anderson, T. A.; Deustua, J. E.; Ghanem, K.; Hait, D.; Hoffmann, M. R.; Lee, S.; Levine, D. S.; Magoulas, I.; Shen, J.; et al. The ground state electronic energy of benzene. *Journal of Physical Chemistry Letters* **2020**, *11*, 8922–8929.
- (51) Löwdin, P.-O. Quantum theory of many-particle systems. I. Physical interpretations by means of density matrices, natural spin-orbitals, and convergence problems in the method of configurational interaction. *Phys. Rev.* **1955**, *97*, 1474.
- (52) Löwdin, P.-O. Quantum theory of cohesive properties of solids. *Adv. Phys.* **1956**, *5*, 1–171.
- (53) Löwdin, P.-O.; Shull, H. Natural orbitals in the quantum theory of two-electron systems. *Phys. Rev.* **1956**, *101*, 1730.
- (54) Davidson, E. R. Properties and uses of natural orbitals. *Rev. Mod. Phys.* **1972**, *44*, 451.
- (55) Zhao, Q.; Zhang, X.; Martirez, J. M. P.; Carter, E. A. Benchmarking an Embedded Adaptive Sampling Configuration Interaction Method for Surface Reactions: H<sub>2</sub> Desorption from and CH<sub>4</sub> Dissociation on Cu (111). *J. Chem. Theory Comput.* **2020**, *16*, 7078.
- (56) Fales, B. S.; Hohenstein, E. G.; Levine, B. G. Robust and efficient spin purification for determinantal configuration interaction. *J. Chem. Theory Comput.* **2017**, *13*, 4162–4172.
- (57) Applencourt, T.; Gasperich, K.; Scemama, A. Spin adaptation with determinant-based selected configuration interaction. *arXiv*, 2018, 1812.06902. <https://arxiv.org/abs/1812.06902>.
- (58) Li Manni, G.; Dobrutz, W.; Bogdanov, N. A.; Guther, K.; Alavi, A. Resolution of Low-Energy States in Spin-Exchange Transition-Metal Clusters: Case Study of Singlet States in  $[\text{Fe}(\text{III})4\text{S}]$  Cubanes. *J. Phys. Chem. A* **2021**, *125* (22), 4727–4740.
- (59) White, S. R. Density-matrix algorithms for quantum renormalization groups. *Phys. Rev. B* **1993**, *48*, 10345–10356.
- (60) Wouters, S.; Van Neck, D. The density matrix renormalization group for ab initio quantum chemistry. *Eur. Phys. J. D* **2014**, *68*, 272.
- (61) Szalay, S.; Pfeffer, M.; Murg, V.; Barcza, G.; Verstraete, F.; Schneider, R.; Legeza, O. *Int. J. Quantum Chem.* **2015**, *115*, 1342.
- (62) Yanai, T.; Kurashige, Y.; Mizukami, W.; Chalupský, J.; Lan, T. N.; Saitow, M. *Int. J. Quantum Chem.* **2015**, *115*, 283–299.
- (63) Baiardi, A.; Reiher, M. The density matrix renormalization group in chemistry and molecular physics: Recent developments and new challenges. *J. Chem. Phys.* **2020**, *152*, 040903.
- (64) Kurashige, Y.; Chan, G. K.-L.; Yanai, T. Entangled quantum electronic wavefunctions of the Mn<sub>4</sub>CaO<sub>5</sub> cluster in photosystem II. *Nat. Chem.* **2013**, *5*, 660–666.
- (65) Li, Z.; Li, J.; Dattani, N. S.; Umrigar, C.; Chan, G. K.-L. The electronic complexity of the ground-state of the FeMo cofactor of nitrogenase as relevant to quantum simulations. *J. Chem. Phys.* **2019**, *150*, 024302.
- (66) Li, Z.; Guo, S.; Sun, Q.; Chan, G. K.-L. Electronic landscape of the P-cluster of nitrogenase as revealed through many-electron quantum wavefunction simulations. *Nat. Chem.* **2019**, *11*, 1026–1033.
- (67) Legeza, Ö.; Sólyom, J. Optimizing the density-matrix renormalization group method using quantum information entropy. *Phys. Rev. B* **2003**, *68*, 195116.
- (68) Legeza, Ö.; Röder, J.; Hess, B. A. Controlling the accuracy of the density-matrix renormalization-group method: The dynamical block state selection approach. *Phys. Rev. B* **2003**, *67*, 125114.
- (69) Moritz, G.; Hess, B.; Reiher, M. *J. Chem. Phys.* **2005**, *122*, 024107.

- (70) Fertitta, E.; Paulus, B.; Barcza, G.; Legeza, Ö. Investigation of metal-insulator-like transition through the ab initio density matrix renormalization group approach. *Phys. Rev. B* **2014**, *90*, 245129.
- (71) Krumnow, C.; Veis, L.; Legeza, O.; Eisert, J. Fermionic Orbital Optimization in Tensor Network States. *Phys. Rev. Lett.* **2016**, *117*, 210402.
- (72) Olivares-Amaya, R.; Hu, W.; Nakatani, N.; Sharma, S.; Yang, J.; Chan, G. K.-L. The ab-initio density matrix renormalization group in practice. *J. Chem. Phys.* **2015**, *142*, 034102.
- (73) Zgid, D.; Nooijen, M. The density matrix renormalization group self-consistent field method: Orbital optimization with the density matrix renormalization group method in the active space. *J. Chem. Phys.* **2008**, *128*, 144116.
- (74) Ghosh, D.; Hachmann, J.; Yanai, T.; Chan, G. K.-L. Orbital optimization in the density matrix renormalization group, with applications to polyenes and  $\beta$ -carotene. *J. Chem. Phys.* **2008**, *128*, 144117.
- (75) Zgid, D.; Nooijen, M. Obtaining the two-body density matrix in the density matrix renormalization group method. *J. Chem. Phys.* **2008**, *128*, 144115.
- (76) Sharma, S.; Chan, G. K.-L. Spin-adapted density matrix renormalization group algorithms for quantum chemistry. *J. Chem. Phys.* **2012**, *136*, 124121.
- (77) Wouters, S.; Poelmans, W.; Ayers, P. W.; Van Neck, D. CheMPS2: A free open-source spin-adapted implementation of the density matrix renormalization group for ab initio quantum chemistry. *Comput. Phys. Commun.* **2014**, *185*, 1501–1514.
- (78) Keller, S.; Reiher, M. Spin-adapted Matrix Product States and Operators. *J. Chem. Phys.* **2016**, *144*, 134101.
- (79) Zhang, N.; Hayase, T.; Kawamata, H.; Nakao, K.; Nakajima, A.; Kaya, K. Photoelectron spectroscopy of iron-sulfur cluster anions. *J. Chem. Phys.* **1996**, *104*, 3413–3419.
- (80) Nakajima, A.; Hayase, T.; Hayakawa, F.; Kaya, K. Study on iron-sulfur cluster in gas phase: electronic structure and reactivity. *Chemical physics letters* **1997**, *280*, 381–389.
- (81) Wang, X.-B.; Niu, S.; Yang, X.; Ibrahim, S. K.; Pickett, C. J.; Ichiye, T.; Wang, L.-S. Probing the intrinsic electronic structure of the cubane [4Fe-4S] cluster: Nature's favorite cluster for electron transfer and storage. *J. Am. Chem. Soc.* **2003**, *125*, 14072–14081.
- (82) Waters, T.; Wang, X.-B.; Wang, L.-S. Electrospray ionization photoelectron spectroscopy: Probing the electronic structure of inorganic metal complexes in the gas-phase. *Coordination chemistry reviews* **2007**, *251*, 474–491.
- (83) DeRossa, D. E.; Chilkuri, V. G.; Van Stappen, C.; Bill, E.; Mercado, B. Q.; DeBeer, S.; Neese, F.; Holland, P. L. Planar three-coordinate iron sulfide in a synthetic [4Fe-3S] cluster with biomimetic reactivity. *Nat. Chem.* **2019**, *11*, 1019–1025.
- (84) Pipek, J.; Mezey, P. G. A fast intrinsic localization procedure applicable for abinitio and semiempirical linear combination of atomic orbital wave functions. *J. Chem. Phys.* **1989**, *90*, 4916–4926.
- (85) Sharma, P.; Truhlar, D. G.; Gagliardi, L. Magnetic Coupling in a Tris-hydroxo-Bridged Chromium Dimer Occurs through Ligand Mediated Superexchange in Conjunction with Through-Space Coupling. *J. Am. Chem. Soc.* **2020**, *142*, 16644–16650.
- (86) Holmes, A. A.; Tubman, N. M.; Umrigar, C. Heat-Bath Configuration Interaction: An Efficient Selected Configuration Interaction Algorithm Inspired by Heat-Bath Sampling. *J. Chem. Theory Comput.* **2016**, *12*, 3674–3680.
- (87) Li, J.; Otten, M.; Holmes, A. A.; Sharma, S.; Umrigar, C. J. Fast semistochastic heat-bath configuration interaction. *J. Chem. Phys.* **2018**, *149*, 214110.
- (88) Apra, E.; Bylaska, E. J.; De Jong, W. A.; Govind, N.; Kowalski, K.; Straatsma, T. P.; Valiev, M.; van Dam, H. J.; Alexeev, Y.; Anchell, J.; et al. NWChem: Past, present, and future. *J. Chem. Phys.* **2020**, *152*, 184102.
- (89) Werner, H.-J. et al. *MOLPRO, version 2015.1, a package of ab initio programs*, 2015.
- (90) Werner, H.-J.; Knowles, P. J.; Knizia, G.; Manby, F. R.; Schütz, M. Molpro: a general-purpose quantum chemistry program package. *Wiley Interdisciplinary Reviews: Computational Molecular Science* **2012**, *2*, 242–253.
- (91) Shao, Y.; Gan, Z.; Epifanovsky, E.; Gilbert, A. T.; Wormit, M.; Kussmann, J.; Lange, A. W.; Behn, A.; Deng, J.; Feng, X.; et al. Advances in molecular quantum chemistry contained in the Q-Chem 4 program package. *Mol. Phys.* **2015**, *113*, 184–215.
- (92) Neese, F. The ORCA program system. *Wiley Interdisciplinary Reviews: Computational Molecular Science* **2012**, *2*, 73–78.
- (93) Neese, F. Software update: the ORCA program system, version 4.0. *Wiley Interdisciplinary Reviews: Computational Molecular Science* **2018**, *8*, e1327.
- (94) Averill, B.; Herskovitz, T.; Holm, R.; Ibers, J. A. Synthetic analogs of the active sites of iron-sulfur proteins. II. Synthesis and structure of the tetra [mercapto- $\mu$ -3-sulfido-iron] clusters, [Fe<sub>4</sub>S<sub>4</sub>(SR)<sub>4</sub>]<sup>2-</sup>. *J. Am. Chem. Soc.* **1973**, *95*, 3523–3534.
- (95) Que, L., Jr; Bobrik, M.; Ibers, J. A.; Holm, R. Synthetic analogs of the active sites of iron-sulfur proteins. VII. Ligand substitution reactions of the tetranuclear clusters [Fe<sub>4</sub>S<sub>4</sub>(SR)<sub>2</sub>]<sup>2-</sup> and the structure of bis (tetramethylammonium)[tetra- $\mu$ -sulfide-tetrakis (benzenethiolato) tetrairon]. *J. Am. Chem. Soc.* **1974**, *96*, 4168–4178.
- (96) Zhang, N.; Liu, W.; Hoffmann, M. R. Iterative configuration interaction with selection. *J. Chem. Theory Comput.* **2020**, *16*, 2296–2316.
- (97) Zener, C. Interaction between the d-shells in the transition metals. II. Ferromagnetic compounds of manganese with perovskite structure. *Phys. Rev.* **1951**, *82*, 403.
- (98) Anderson, P. W.; Hasegawa, H. Considerations on double exchange. *Phys. Rev.* **1955**, *100*, 675.
- (99) de Gennes, P.-G. Effects of double exchange in magnetic crystals. *Phys. Rev.* **1960**, *118*, 141.
- (100) Boguslawski, K.; Tecmer, P. Orbital entanglement in quantum chemistry. *Int. J. Quantum Chem.* **2015**, *115*, 1289–1295.
- (101) Guo, Y.; Zhang, N.; Lei, Y.; Liu, W. iCISCF: An Iterative Configuration Interaction-based Multiconfigurational Self-consistent Field Theory for Large Active Spaces. *arXiv*, 2021, 2106.10223. <https://arxiv.org/abs/2106.10223>.
- (102) Cao, L.; Ryde, U. Extremely large differences in DFT energies for nitrogenase models. *Phys. Chem. Chem. Phys.* **2019**, *21*, 2480–2488.
- (103) Wei, H.; Wang, B.; Chen, Z. SMagnetic exchange of trinuclear spin frustration system: CASPT2 and density functional theory study on hydroxo-bridged chromium complex [Cr<sub>3</sub>(NH<sub>3</sub>)<sub>10</sub>(OH)<sub>4</sub>]<sup>+</sup>·Br<sup>-</sup>. *Chem. Phys. Lett.* **2005**, *407*, 147–152.
- (104) Massolle, A.; Neugebauer, J. Subsystem density-functional theory for interacting open-shell systems: spin densities and magnetic exchange couplings. *Faraday Discuss.* **2020**, *224*, 201.